

UNIVERSITY OF SOUTHAMPTON

**Applications of Microfluidics in Nuclear  
Magnetic Resonance**

by

William G Hale

A thesis submitted in partial fulfillment for the  
degree of Doctor of Philosophy

in the  
Faculty of Engineering and Physical Sciences  
School of Chemistry

31/07/2019

UNIVERSITY OF SOUTHAMPTON

ABSTRACT

FACULTY OF ENGINEERING AND PHYSICAL SCIENCES  
SCHOOL OF CHEMISTRY

Doctor of Philosophy

by William G Hale

Microfluidics is a constantly growing field of research, finding applications in a diverse range of subjects such as materials science, chemistry and across the life sciences. This expansion is due to many advantageous attributes: small sample volumes which contribute to waste reduction and reduced cost of experimentation; highly controllable local environments that enable very precise investigation of changes in systems to stimuli; rapid prototyping techniques that mean make, test, tweak cycles can be run more than once in a typical day; ease of parallelisation makes gathering statistically significant data much easier without the need to repeat experiments for days at a time; and ease of automation increases precision and repeatability.

Nuclear magnetic resonance (NMR) spectroscopy is a widely applied technique in chemistry and the life sciences. Its non-invasive and non-destructive nature makes NMR ideal to study living, or mass limited samples. NMR, however, requires an extremely homogenous magnetic field to enable molecular structure determination and can be limited by the inherent low sensitivities possible in a typical experiment.

This thesis describes methods for integrating these two fields. Some NMR experiments being ‘miniaturised’ to be performed ‘on-chip’ as well as microfluidic concepts that have been engineered to be compatible with NMR techniques. These techniques do not seek to replace established methods of microfluidic analysis such as mass spectrometry or fluorescence spectroscopy but could be used to compliment these techniques as an additional method of extracting data from a system.

# Contents

<b>Nomenclature</b>	<b>v</b>
<b>Acknowledgements</b>	<b>viii</b>
<b>1 Background</b>	<b>1</b>
1.1 Microfluidics	1
1.1.1 History to present day	1
1.2 Quantum Theory of Nuclear Magnetic Resonance	10
1.2.1 Nuclear Spin	10
1.2.2 Spin Systems	10
1.2.3 Pauli matrices and more operators	13
1.2.4 Density Operator	15
1.2.5 The Hamiltonian	19
1.2.5.1 Spins in a magnetic field	19
1.2.6 Spin precession	21
1.2.7 Rotating Frame	22
1.2.7.1 Precession in the rotating frame	23
1.2.8 Radio Frequency Pulses	23
1.2.8.1 $x$ -pulse	24
1.2.8.2 Pulse of general phase	25
1.2.8.3 Off-resonance effects	26
1.2.9 The Density operator revisited	27
1.2.9.1 Magnetization vector	28
1.2.9.2 Density operator under pulses	29
1.2.10 Free evolution with relaxation	30
1.2.10.1 Transverse relaxation	31
1.2.10.2 Longitudinal relaxation	32
1.2.11 NMR signal and detection	32
1.2.11.1 Quadrature detection	34
1.2.11.2 Signal after a pulse	36
1.2.11.3 Chemical Shift and J-coupling	37
1.3 Micro-NMR	39
1.3.1 Sensitivity	39
1.3.1.1 Signal to noise ratio	39
1.3.2 Signal Averaging	41
1.3.3 Limit of Detection	43
1.3.4 Concentration limit of detection	43

---

1.3.5	Transmission line probe . . . . .	44
-------	-----------------------------------	----

## Abbreviations

<b>Acronym</b>	<b>Definition</b>
cLOD	Concentration Limit of Detection
dDNP	dissolution Dynamic Nuclear Polarization
DNP	Dynamic Nuclear Polarization
DTPA	Diethylenetriaminepentaacetic Acid
EMF	Electromotive Force
FCC	Face-Centred Cubic
FID	Free Induction Decay
HMQC	Heteronuclear Multiple Quantum Coherence
LIF	Laser Induced Fluorescence
LoC	Lab-on-a-chip
MAS	Magic Angle Spinning
MR	Magnetic Resonance
MRI	Magnetic Resonance Imaging
nLOD	Mass Limit of Detection
NMR	Nuclear Magnetic Resonance
OTC	Oxytetracycline
PDMS	Poly(dimethylsiloxane)
PHIP	Parahydrogen Induced Polarization
PMMA	Poly(methylmethacrylate)
ppm	Parts Per Million
PTFE	PolyTetraFluoroEthylene
r.f.	Radio Frequency
RF	Radio Frequency
RMS	Root Mean Square
SABRE	Signal Enhancement By Reversible Exchange
SNR	Signal to Noise Ratio
SPR	Surface Plasmon Resonance
TLP	Transmission Line Probe
TOCSY	Total Correlation Spectroscopy
UV-light	Ultraviolet-light
2D	Two Dimensional
3D	Three Dimensional
$\mu$ TAS	Micro Total Analysis System

# Nomenclature

$a$	The signal amplitude
$\mathbb{B}$	The Boltzmann factor
$B_0$	The external magnetic field
$B_1$	The magnetic field produced by an NMR coil
$c_s$	The concentration of spins in a sample
$C$	A constant in SNR
$d$	The coil diameter
$F$	The noise factor from the spectrometer
$\mathbf{H}$	The magnetic field
$h$	Planck's constant
$\hbar$	The reduced Planck constant
$\hat{H}$	The Hamiltonian operator in natural units
$I$	The spin quantum number
$\hat{I}$	The spin angular momentum operator
$i_c$	The current
$J$	The rotational quantum number
$k_0$	A constant that accounts for spatial inhomogeneities in the $B_1$ field
$k_B$	The Boltzmann constant
$l$	The length of a coil
$M_0$	The net magnetisation
$M_a$	The magnetisation vector component along the $a$ -axis
$\mathbf{M}$	The magnetisation
$n_s$	The number of spins in a sample
$\tilde{\mathbf{n}}$	The surface normal
$p$	The polarisation of a spin system
$P_\alpha$	The population of the $\alpha$ state
$R_{\text{noise}}$	The dissipative losses
$\hat{R}$	The rotation operator
$S(t)$	The signal in the time domain
$S(\Omega)$	The signal in the frequency domain
$T$	The absolute temperature
$T_s$	the singlet relaxation time constant

---

$T_1$	The longitudinal relaxation time constant
$T_2$	The transverse relaxation time constant
$U$	The scalar magnetic potential
$V_s$	The sample volume
$V'_s$	The product of $k_0$ and $V_s$ that is the volume is within 10% of maximum
$\mathbb{1}$	The identity matrix
$\alpha_F$	The filling factor
$\beta_p$	The tilt of the roatation axis from $z$ for an off-resonance pulse
$\gamma_j$	The gyromagnetic ratio for a nucleus, $j$
$\delta$	The chemical shift
$\delta_{\text{RF}}$	The RF current penetration depth
$\Delta f$	The spectral bandwidth
$\epsilon$	The enhancement factor
$\theta$	The tilt angle of magnetisation
$\theta_{\text{RF}}$	The angle between the r.f. coil and $B_0$
$\lambda_l$	The decay constant of a spin $l$
$\mu$	The reduced mass
$\mu_0$	The vacuum permeability
$\hat{\mu}$	The magnetic dipole moment operator
$\xi$	The emf
$\rho_r$	The resistivity
$\hat{\rho}$	The density operator
$\sigma$	The chemical shielding factor
$\sigma_{\text{noise}}$	The root mean square noise
$\phi_p$	The phase of an r.f. pulse
$\phi_{\text{ref}}$	The phase shift in the rotating frame
$\Phi$	The angle that connects the static to rotating frame
$\chi_V$	The Magnetic susceptibility
$\omega_j^0$	The larmour frequency for a nucleus, $j$
$\omega_{\text{nut}}$	The nutation frequency
$\omega_{\text{ref}}$	The rotating frame frequency
$\Omega^0$	The and rotating frame frequency offset

## Declaration of Authorship

This thesis is the result of work done wholly while I was in registered candidature for a Ph.D. degree at the University of Southampton. The material presented here is based on work mostly done by myself. Where the work was carried out jointly with others, a substantial part is my own original work and co-workers and their roles have been clearly indicated. The material contained herein has not been submitted by the author for a degree at any other institution.

Signed:

31/07/2019



## Acknowledgements

I would like to express my deep gratitude to Professor Marcel Utz for providing patient guidance and enthusiastic encouragement, as well as engaging discussion concerning all matters of life and work. His depth of knowledge in all manner of subjects was a great help throughout my PhD and provided a seemingly endless source of ideas and problem solving. The principles of scientific investigation I have learnt from him will stay with me throughout my career.

I wish to thank Professor Malcolm Levitt for his support and guidance, the discussions we have had about science helped me to see problems in a different light and increased my effectiveness as a scientist.

I am grateful to my colleagues who have helped me enormously throughout my time in Southampton in no particular order I wish to thank: James Eills, Graeme Finch, Rachel Greenhalgh, Benno Meir, Javier Alonso-Valdesueiro, Karel Kouril, Hana Kourilova, Aliko Moysiadi, Stuart Elliot, Christian Bengs, Manvendra Sharma, Bishnubatra Partra, Matheus Rossetto, Gabriel Rossetto, Marek Plata, Sylwia Ostrowska, Weidong Gong, Mohammed Sabba, George Bacanu, Laurynas Dagys, Jo Collet and Barbara Ripka.

To the people that provided support and encouragement throughout my work and helped me keep sane, I am indebted to Frankie Leeming, Thomas Kear, Laura Jowett, James Eills, Stuart Elliot, Christian Bengs, Aliko Moysiadi, Nic Charles, Judy Fox, Josie Charles, Gemma Charles and Eddie Robinson you all helped immensely.

In particular I'd like to thank Alyssa Charles for her unwavering support, encouragement, and belief in me, as well as proof reading and correcting my grammar errors.

Finally, I'd like to thank my family for all their support over the years, this is only possible because of them.

*To my friends and family*

# Chapter 1

## Background

### 1.1 Microfluidics

#### 1.1.1 History to present day

The first analytical miniaturised device fabricated on silicon was presented in 1979 by Terry *et al* [1]. This device, was a gas chromatograph capable of separating a simple mixture of gases in seconds, and included an injection valve and a 1.5 m long separation column. A thermal conductivity detector was fabricated separately, and clamped to the silicon wafer containing the column. This subsequently allowed for a reduction in size of the chromatograph of nearly 3 orders of magnitude compared to the conventional lab equipment at the time, and is regarded as the first demonstration of the power of miniaturisation from which, the field of lab-on-a-chip and microfluidics would be born [2]. Into the 1980s, research related to miniaturisation focused on the fabrication of components, like micropumps [3, 4], and microvalves [5] rather than silicon based analysers.

In 1990, work describing a miniaturised liquid chromatograph on a silicon wafer was published [6]. This work described a 5 x 5 mm chip containing a column and detector that was connected to an off-chip HPLC pump and valves, enabling it to perform high pressure liquid chromatography. Concurrently, the concept of a 'miniaturised total analysis system' ( $\mu$ TAS) was introduced by Manz *et al* [7], where the incorporation of sample pretreatment, separation, and detection onto a single device was proposed to enhance the analytical performance of the device, rather than simply reduce its size. However, it was also recognised that miniaturisation of the device presented the advantage of not only a smaller consumption of materials, but would also enable the integration of multiple separation techniques capable of monitoring many components in a single device.

Such a device was envisioned as capable of sample handling, analysis, detection, and incorporating control of mass transport. Conventional pumps at the time struggled

with the high pressures needed for transport in small channels, and early theoretical considerations showed that electroosmotic pumping was an attractive and feasible way to move aqueous liquid through a  $\mu$ TAS, especially when separation was needed.

Electroosmosis is defined as the motion of liquid induced by an applied potential. An electroosmotic pump has no moving parts and produces an even flow along the entire length of the channel, ideal for early applications of  $\mu$ TAS that imagined separating and analysing aqueous solutions. Early efforts were first put into optimising injection and separation of liquids by switching voltages between the reservoirs containing reagent, carrier and waste [8].

Electrophoresis in a  $\mu$ TAS was reported in 1992 using silicon and glass [9]. This demonstrated success in using electroosmotic pumping for flow control in interconnected channels, without the use of valves, as well as the concept of integrating injection, separation, and detection into a single device. As electrophoresis was most commonly used to separate biological samples, usually charged molecules in aqueous solution, it could be used to detect amino acids separated on-chip, using laser induced fluorescence [10]. In addition to separation of biological samples, applications of reactions concerning biomolecules and the handling of cells also started to emerge.

Microfabricated device capability started to become more complicated and microfluidics found uses in DNA amplification by polymerase chain reaction (PCR) [11] and cellular metabolism [12]. As analysis of biological samples in water became available, fabrication of the devices from glass and silicon became unnecessary and inappropriate. Silicon was at the time expensive, but more importantly, opaque to visible and UV-light, and so couldn't be used with conventional methods of optical detection frequently used in biology. The increasing complexity of the devices also meant it became important for pumps and valves to be integrated into the device and these are more easily made from elastomers than silicon or other rigid materials. The trend towards studying mammalian cells lead to different requirements such as gas permeability, which neither glass or silicon can provide. It was for these reasons that the replacement of silicon and glass with polymers was required [13].

Poly(dimethylsiloxane) (PDMS) was the polymer of choice, the properties of which differ greatly from silicon or glass [14, 15]. The switch to PDMS was made even more attractive by the development of soft-lithography as a method for building prototype devices [16], and the development of a method to fabricate pneumatically actuated valves, pumps, and mixers [16]. These advances are only possible due to the elastomeric nature of PDMS and would not be possible with a pure silicon or glass devices. The improved methods of fabrication lead to the creation of the components required for more sophisticated experiments in the form of: valves that enabled immunoassays (Fig. 1.1) [17]; an integrated microfluidic system for efficient mixing [18]; and pumps [19]. With

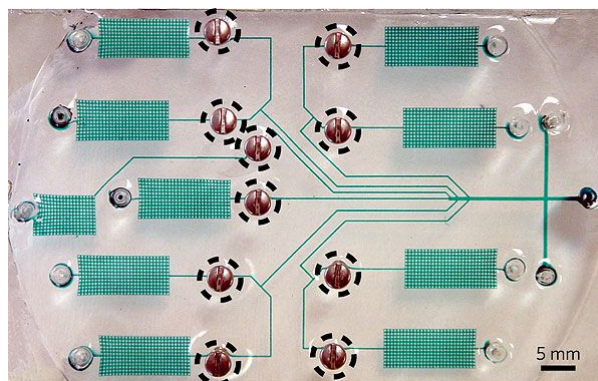


FIGURE 1.1: Components of a microfluidic device got increasingly complicated. This device from Ref.[17] performs immunoassays - widely used in medical and biological research. The screws (dashed circles) are manually operated valves. Water with green dye shows the channels.

these components, microfluidics was in a position to tackle more complex problems, one example of this is shown in Fig. 1.1.

As these fabrication methods become more widely used, the field of microfluidics moved from adding components to its analytical arsenal, to starting to find applications for devices. Microfluidic devices then found applications in protein crystallisation [20], separations coupled with mass spectroscopy [21], single cell manipulation [22], and synthesis of  $^{19}\text{F}$ -labelled organic compounds for use in PET scans [23].

A subsection of microfluidics began to emerge around this time too, as low Reynolds numbers make multiphase flow manipulation relatively easy, the generation and manipulation of droplets [24–26] then began to be explored. These experiments involved dispersing a liquid phase in a continuous liquid stream to form a monodisperse emulsion of (often) aqueous droplets in oil. These droplets were used to produce polymer particles [27], in making irregular particles [28], hollow microcapsules [29], and protein detection in cells [30]. An example of one of the ways droplets were first produced in microfluidic devices is shown in Fig. 1.2.

In parallel, another branch of microfluidics was being developed, its goal was to culture cells in a repeatable way. In their normal environment, cells are subject to multiple cues including cytokines and other signalling molecules from neighbouring cells, biochemical interactions with the extracellular matrix, mechanical stress, and direct cell to cell contacts. Microfluidics was seen as an ideal method of providing cells with these cues, in a controlled and reproducible fashion that couldn't be easily replicated with conventional cell culture. By using microfluidic devices one can combine cell culture with analytical techniques in order to probe the biochemical processes that govern cell behaviour.

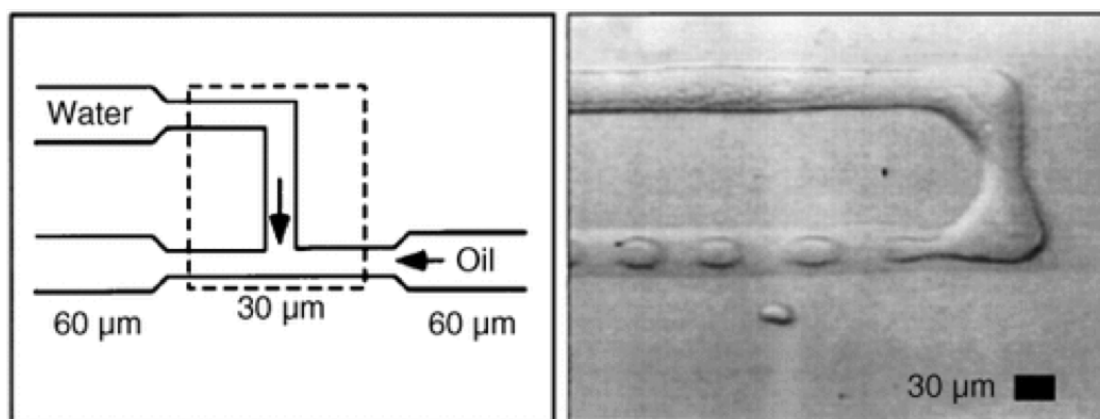


FIGURE 1.2: Formation of droplets in a T-Junction of a microfluidic device the continuous hydrocarbon phase disperses a water phase. Figure from [31]

Microfluidic devices have been used to enable cell-based assays, from culturing cells to biochemical analysis. In Fig. 1.3 images of different devices are shown that convey how complex the devices being produced were becoming. Despite integration of functionalities proving difficult, these demonstrate the power of miniaturisation and the ingenuity being developed in the field. Microfluidics can offer unique control over cell-cell and soluble cues, typical of *in vivo* cell environments, by combining microfabrication of 3D extracellular matrix (ECM) structures and fluid networks capable of delivering nutrients and oxygen [44].

Throughout the 2000s, microfabrication, which combined micropatterning techniques such as photolithography, photo-reactive chemistry, and soft lithography, made it possible to engineer the microenvironment of the cell on similar length scales to the cell itself [45]. This surface patterning of micro-metre sized features enabled control of cell-ECM interactions, and was used to fabricate 3D scaffolds on which to grow cells that were made of biodegradable materials [46].

One area of application was the 3D culture of liver cells. *In vitro* culture of liver cells is of particular interest as many drugs fail clinical studies because they either damage the liver directly, or because the metabolites produced by the liver are toxic [47]. Efforts were made to produce *in vitro* culture systems that mimic real liver conditions. In the liver, hepatocytes are found in a complex 3D environment in which nutrients, soluble factors and oxygen, are transported through blood capillaries and bile canaliculi. This 3D environment often contains polar tissue structure where the two sides of the cell are exposed to different media, for example, in the liver some hepatocytes are exposed to the bile on one side and blood on the other, which is hard to reproduce using 2D cell culture alone. Using silicon as a substrate, Powers *et al.* fabricated 3D liver reactors using array of 300  $\mu\text{m}$  wide channels [48]. In their device they perfused rat liver cells providing fluid shear stresses within physiological range and found that the cells seeded into the channels rearranged extensively to form 'tissue like' structures, and remained viable for up to 2 weeks.

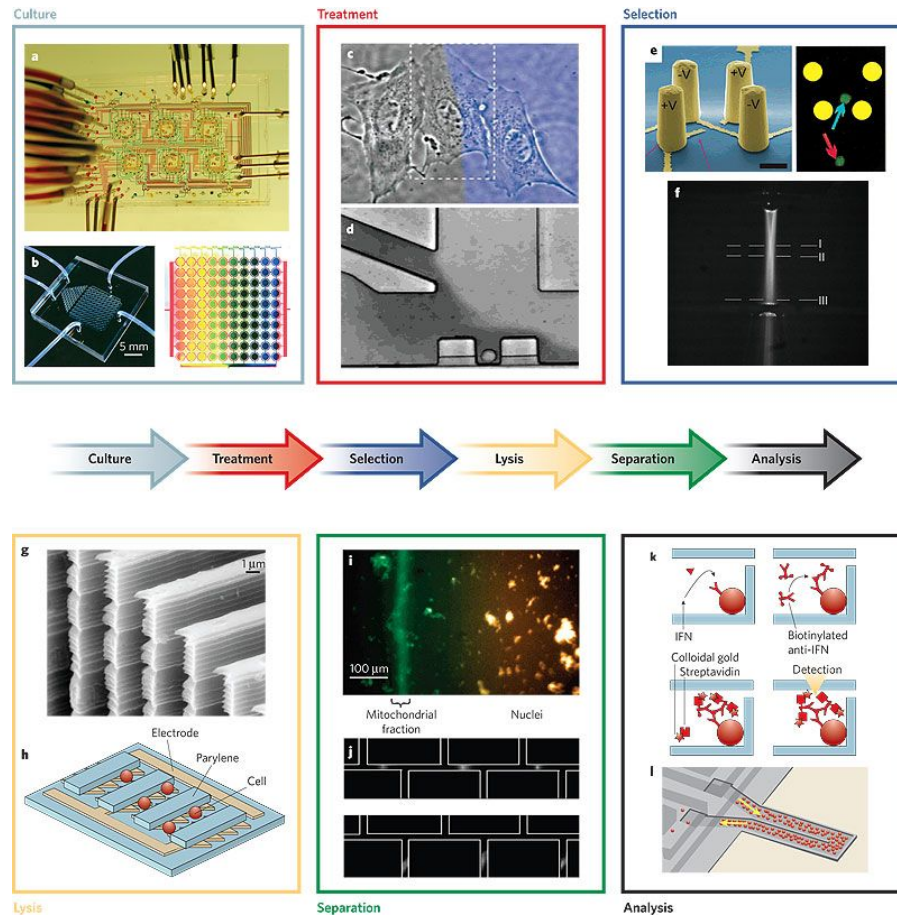


FIGURE 1.3: A collection of microfluidic devices that enabled cell based assays from cell culture, to selection and treatment, to analysis. **a**, Six bioreactors are operated in parallel in a single chip to monitor small numbers of cells [32], **b**, Microfluidic cell-culture array with integrated concentration gradient generator (left). Image of concentration gradient when blue and yellow dye is used (right) [33]. **c** Two laminar streams exposing two sides of a single cell to different conditions [34]. **d**, Perfusion over a single trapped cell. The perfusion media can be switched in 100 ms [22]. **e**, (left) Cell dielectrophoresis trap. (right) Fluorescent image of trapped cell indicated by blue arrow [35]. **f**, Fluorescent image of light path at the detection zone in a micro flow cytometer [36]. **g** Scanning electron micrograph of a mechanical lysis device with sharp knife-like protrusions [37]. **h**, Schematic of electrical lysis device with microelectrodes [38]. **i**, Isoelectric focusing of cell organelles [39]. **j**, Two-dimensional separation of four model proteins. Isoelectric focusing (top) followed by SDS gel electrophoresis [40]. **k**, Schematic of immunoassay using microbeads as a solid support [41]. **l**, Schematic of a hollow cantilever-based mass sensor for analyte detection [42]. Taken from Ref.[43]



Later, Sivaraman *et al.* developed a different system to culture liver cells in a 3D scaffold using polycarbonate housing for a silicon device. This device contained microfabricated wells in which the cells were seeded and perfused with media. They also observed that the cells in the 3D culture had cell-cell contacts that resembled those found in tissues *in vivo* [47]. It has been observed that co-culture of hepatocytes with other cell types, including liver epithelial cells and Kupffer cells, prolongs the survival of cultured hepatocytes and helps maintain liver-specific properties such as albumin secretion [49].

As 3D cell culture became more widely used, a new sub-genre of microfluidics was formed, organ-on-a-chip. Early efforts had shown that microfabrication of adhesive substrates provided well-controlled environments for cell growth and expression of differentiated tissue-specific functions [50, 51]. Advances in soft lithography-based microfluidic devices made it easier to develop the more complex 3D architecture of living tissues and organs. For example, a poly(dimethylsiloxane) (PDMS) device was developed that contained structures which mimic the structure of the endothelial-epithelial interface that forms the liver sinusoid [52].

Along with liver function, kidney, lung, and body functions were replicated in microfluidic devices shown in Fig. 1.4. Whilst the liver and kidney offer highly simplified micro-engineered models, within organs, *in vivo* nutrients, hormones, metabolites, cytokines and physical signals are usually transferred across interfaces between adjacent living cells, and therefore require a much more complex microenvironment for true replication. Huh *et al.* created a model of the human alveolar-capillary interface, formed in a flexible PDMS device containing a central channel and two hollow side chambers [53]. A 10  $\mu\text{m}$  thick PDMS membrane containing an ordered array of micropores (10  $\mu\text{m}$  diameter) was stretched across the central channel, splitting it in two, see Fig. 1.4. Human alveolar epithelial cells were then cultured on one side of the membrane and exposed to air, while human lung capillary endothelial cells were cultured on the opposing side and exposed to flowing medium. When the hollow side chambers were exposed to vacuum, the cells were subjected to strain ranging from 5%-15% to match strain observed within whole lung *in vivo*. In doing so, they found their 'lung on a chip' accentuated the inflammatory responses of the cells to silica nanoparticles. This mechanical strain also enhanced uptake of nanoparticles and stimulated the transport into the vascular channel, and similar effects of physiological breathing were observed in whole mouse lung. These early organ-on-a-chip experiments paved the way for more complex 'Body-on-a-chip' devices. Body-on-a-chip devices contain multiple types of cultured cells connected by a network of microfluidic channels, which permit recirculation and exchange of metabolites in a physiologically-relevant manner [54]. These devices have found applications in drug screening and disease modelling [55].

As the complexity of cell culture within microfluidic devices increased, so to, did the detection methods. Coupling a detector to an LOC is critical for any analytical purpose. A number of detector technologies were demonstrated in microfluidic devices,



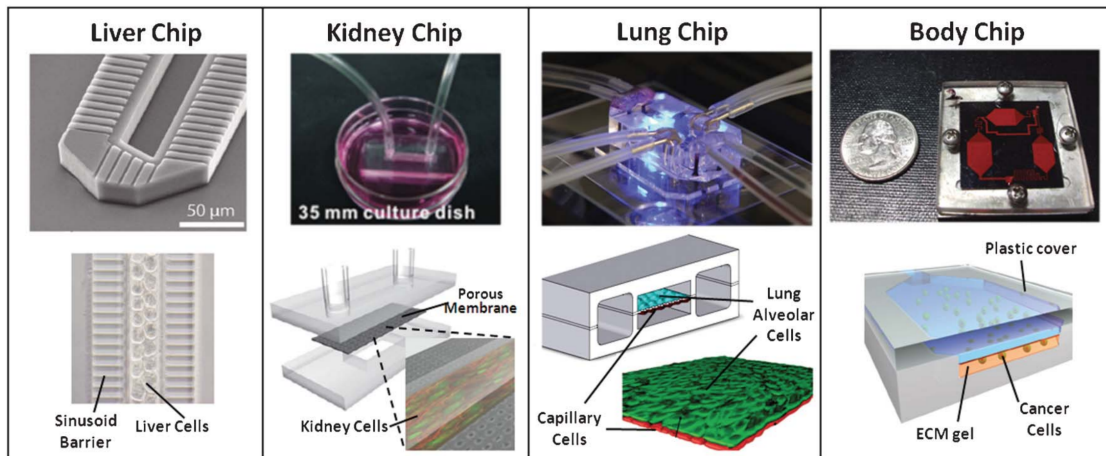


FIGURE 1.4: Organ-Organ and tissue-tissue interfaces in microdevices. Liver chip: A microfluidic liver device with cell culture and flow chambers separated by a baffle that separates cultured hepatocytes from fluid flow to simulate the endothelial-hepatocyte interface of the liver sinusoid. This geometry promotes alignment of hepatocytes in two lines that facilitates the production of functional bile canaliculi along hepatic-cord-like structures [52]. Kidney chip: A simple kidney on a chip that mimics the interface between epithelium and flowing urine was created by bonding a PDMS well and a PDMS channel to either side of a semi-permeable membrane on which cells are cultured and subjected to fluid flow [56]. Lung chip: A lung-on-a-chip capable of replicating mechanical strain caused by breathing, fabricated from PDMS that mimics the physiological function of the alveolar-capillary interface in the human lung. The hollow chambers are subjected to cyclic suction to replicate breathing movements whilst fluid flowing mimics blood flow [53]. Body chip: A microfluidic device containing multiple linked tissue types representing different organs was constructed by sealing three cell culture chambers against a cover. Each cell culture chamber contains a 3D ECM gel containing living cells from a different organ. Media was circulated through the chambers via microfluidic channels during operation [57]. Figure taken from [58].

including electrochemical [59], mechanical [60], and optical methods [61]. The small sample volumes typical to a microfluidic experiment are an important challenge to overcome for any detector, ideally, they should be highly sensitive and scalable to smaller dimensions.

The mechanism and features of the detection technologies are summarised in [62] and reproduced in Table 1.1.1.

Method	Mechanism	Features
Electrochemical	Measures changes in conductance, resistance and/or capacitance at the active surface of the electrodes	(+) Real-time detection, (+) Low-cost microelectrode fabrication, (-) Control of ionic concentrations before detection, (-) Short shelf life
Mechanical	Detection is based on variations of the resonant frequency or surface stress of the mechanical sensor	(+) Monolithic sensor integration, (+) Label free detection, (-) damping effects in liquid samples, (-) Detection takes time ( 30 mins), (-) Complex fabrication
Optical	Detects variations in light intensity, refractive index sensitivity, or interference pattern	(+) Minimal sample preparation, (+) Real-time detection, (+) Ubiquitous in laboratories, (-) Conventional instrumentation is expensive, (-) Set-up complexity

TABLE 1.1: Summary of electrochemical, mechanical and optimal detection technologies employed in microfluidics.

Electrochemical detection involves the interaction of chemical species with electrodes or probes. This interaction results in a variation of signal, such as potential or current, which enables analysis of target analytes. The electrochemical phenomenon deals with two major effects: (i) chemical reactions are promoted by passing an electrical current through the electrode system; or (ii) electrode responses are triggered due to specific chemical reactions. These effects are usually observed using an electrolytic cell. Reactions of oxidation and reduction occurring at the surface of the electrodes are the basis for electron transfers between the electrolyte (sample) and the electrodes. In a typical electrolytic cell, the electrode system is formed by the working electrode, where detection of a certain analyte is analyzed, and the reference electrode, where a standard oxidation/reduction is conducted [63]. Wongkaew *et al.* reported an electrochemical biosensor that employed a microelectrode array. In the array, adjacent electrode fingers form micro-sized gaps which allow an increase of the diffusion flux of chemical species, thus leading to an enhanced collection efficiency and higher signal amplification. The microchannels of the device were made by hot embossing PMMA and the electrodes were made, by e-beam and wet-etching processes. The detection of targets using this system took 250 seconds and reported limits of detection of 12.5  $\mu\text{M}$ .

Mechanical detection systems mainly used cantilever technology, which showed that it could be accurate when detecting biomolecules [64]. Cantilever-based devices generally operate in two different modes upon analyte binding: (i) static deflection, where binding on one side of a cantilever causes unbalanced surface stress resulting in a measurable deflection; (ii) dynamic, resonant mode, where binding on a cantilever causes

variations of its mass and consequently shifts the resonant frequency. Mechanical-based detection has the advantage that it may require no labelling of biomolecules. Labels often make the detection method more complicated, time-consuming, and costly, and could interfere with the function of biomolecules under investigation. Another characteristic of cantilever technology is the potential to fabricate large arrays of sensors for multi-molecular sensing [65]. Hou *et al* [66] presented a device that contained a micro-fabricated cantilever array for the specific detection of oxytetracycline (OTC), a common broadband antibiotic used in animals, that can accumulate in our food chain and cause side effects in humans. The device achieved this by functionalising the cantilevers with OTC specific DNA aptamers, these bind to the OTC and increase the load on the cantilevers causing them to deflect, and once calibrated can indicate the concentration of OTC in solution. The limit of detection in this case is 0.2 nM in 1000 seconds.

Optical detection is preferred for robust, sensitive, Lab on a chip devices. It has been the most widely used technique for quantitative proteomic analysis [67], and infectious disease diagnostics [68], due in part, to the ubiquity of the optical instrumentation required in biological laboratories, meaning these devices can be used readily in most locations. Conventional optical detection methods, including absorbance [69], chemiluminescence [70], fluorescence [71], and surface plasmon resonance (SPR) [72], have all been applied in microfluidic devices. Foudeh *et al.* [72] developed an SPR microdevice for the detection of *Legionella pneumophila*, which is the pathogenic organism that causes Legionellosis and is responsible for fatality rates of over 10% within hospital and industrial outbreaks [73]. The device is ultra-sensitive to RNA of *Legionella pneumophila* and has a limit of detection of 1 pM in less than 3 hours.

Presently, microfluidics is a large and diverse field, so much so that the areas that started out as sub-categories are now referred to as their own field of research. Indeed, within the last three years, the journal Lab on a Chip has published no less than 116 reviews focusing on a wide variety of applications that microfluidics now enjoys, such as: 3D printed fluidic networks [74]; droplet microfluidics for synthetic biology [75]; phase behaviour characterisation for industrial CO<sub>2</sub>, oil and gas [76]; the production of stem cells using messenger RNAs [77]; and paper microfluidics for diagnosis of malaria in low resource communities [78].

## 1.2 Quantum Theory of Nuclear Magnetic Resonance

### 1.2.1 Nuclear Spin

Nuclei have an intrinsic property known as spin. This spin can be represented by operators along the three Cartesian axes  $\hat{I}_x$ ,  $\hat{I}_y$ , and  $\hat{I}_z$ .

The spin angular momentum operators  $\hat{I}_x$ ,  $\hat{I}_y$  and  $\hat{I}_z$  satisfy cyclic commutation rules:

$$[\hat{I}_x, \hat{I}_y] = i\hbar \hat{I}_z \quad (1.1)$$

$$[\hat{I}_y, \hat{I}_z] = i\hbar \hat{I}_x \quad (1.2)$$

$$[\hat{I}_x, \hat{I}_z] = i\hbar \hat{I}_y. \quad (1.3)$$

The total square angular momentum operator,  $\hat{I}^2$  can be defined as:

$$\hat{I}^2 = \hat{I}_x^2 + \hat{I}_y^2 + \hat{I}_z^2, \quad (1.4)$$

this commutes with the three spin angular momentum operators:

$$[\hat{I}^2, \hat{I}_x] = 0 \quad (1.5)$$

$$[\hat{I}^2, \hat{I}_y] = 0 \quad (1.6)$$

$$[\hat{I}^2, \hat{I}_z] = 0. \quad (1.7)$$

Spin angular momentum operators have eigenstates and eigenvalues. When the operators act on their eigenstate they return the eigenstate multiplied by a scalar eigenvalue. If the nuclear spin quantum number is  $I$ , then the operator  $\hat{I}_z$  has  $2I + 1$  eigenstates,  $m_I$ . States are denoted  $|I, m_I\rangle$  [79] and the angular momentum operator acts according to the following:

$$\hat{I}_z |I, m_I\rangle = m_I \hbar |I, m_I\rangle. \quad (1.8)$$

The total square angular momentum operator acts in the following way:

$$\hat{I}^2 |I, m_I\rangle = I(I + 1)\hbar^2 |I, m_I\rangle, \quad (1.9)$$

where  $I$  can take half-integer and integer values from zero, i.e  $I = 0, \frac{1}{2}, 1, \frac{3}{2}, \dots$ , and  $m_I$  takes one of the integer values from  $-I$  to  $+I$ .

### 1.2.2 Spin Systems

The simplest case that can be considered in NMR is a system of isolated spin-1/2 nuclei.

According to the quantum theory of angular momentum discussed in 1.2.1, a single spin-1/2, when placed in a magnetic field, has two eigenstates of angular momentum along the  $z$ -axis, denoted by  $|\alpha\rangle$  and  $|\beta\rangle$ , and defined as:

$$|\frac{1}{2}, +\frac{1}{2}\rangle = |\alpha\rangle \quad (1.10)$$

$$|\frac{1}{2}, -\frac{1}{2}\rangle = |\beta\rangle. \quad (1.11)$$

The states  $|\alpha\rangle$  and  $|\beta\rangle$  are called the *Zeeman eigenstates* of a spin-1/2 and are acted on by  $\hat{I}_z$  according to the following:

$$\hat{I}_z |\alpha\rangle = +\frac{1}{2}\hbar |\alpha\rangle \quad (1.12)$$

$$\hat{I}_z |\beta\rangle = -\frac{1}{2}\hbar |\beta\rangle, \quad (1.13)$$

Eqn. 1.12 shows that the eigenstate  $|\alpha\rangle$  has an eigenvalue of  $+\hbar/2$  and  $|\beta\rangle$  has an eigenvalue of  $-\hbar/2$ , these are said to be polarised along the  $z$ -axis. This polarization is sometimes represented by up and down arrows pointing along the positive or negative  $z$ -axis, indicating the direction of well-defined spin angular momentum. However, for the same spin, the  $x$  and  $y$  components are fundamentally unpredictable since the states  $|\alpha\rangle$  and  $|\beta\rangle$  are not eigenstates of the operators  $\hat{I}_x$  or  $\hat{I}_y$ . The  $x$ -axis angular momentum is *undefined* as measurements give  $\pm 1/2$  with equal probability and this is very hard to represent in a diagram.

The Zeeman eigenstates can be used to define the Zeeman basis. The two kets,  $|\alpha\rangle$  and  $|\beta\rangle$  can be represented by the column vectors:

$$|\alpha\rangle = \begin{pmatrix} 1 \\ 0 \end{pmatrix} \quad |\beta\rangle = \begin{pmatrix} 0 \\ 1 \end{pmatrix}, \quad (1.14)$$

as well as kets, bras are also defined by taking the conjugate transpose of the ket,  $|\alpha\rangle^\dagger = \langle\alpha|$  such that

$$\langle\alpha| = (1 \quad 0) \quad \langle\beta| = (0 \quad 1). \quad (1.15)$$

The state,  $|\psi\rangle$ , of a two level system can now be completely described in this basis as the linear combination of the basis states:

$$|\psi\rangle = c_1 |\alpha\rangle + c_2 |\beta\rangle = \begin{pmatrix} c_1 \\ c_2 \end{pmatrix} \quad (1.16)$$

$$\langle\psi| = c_1^* \langle\alpha| + c_2^* \langle\beta| = (c_1^* \quad c_2^*). \quad (1.17)$$

These are normalised such that  $c_1 c_1^* + c_2 c_2^* = 1$ .

To complete the picture, the states must be orthonormal. Orthonormality between states exists if the inner product of the basis states  $|r_i\rangle$  and  $|r_j\rangle$  satisfies the following conditions:

$$\langle r_i | r_j \rangle = \delta_{ij}, \quad (1.18)$$

where the Kronecker delta,  $\delta_{ij}$  is:

$$\delta_{ij} = \begin{cases} 0 & \text{if } i \neq j \\ 1 & \text{if } i = j \end{cases}, \quad (1.19)$$

and where  $\langle r_i | r_j \rangle = \delta_{ij}$  denotes taking the dot product between the two vectors  $|r_i\rangle$  and  $|r_j\rangle$ .

The basis states help to quantify the component of a state vector along that state. Take our example from Eqn. 1.16, inner products of the overall state,  $|\psi\rangle$  with  $|\alpha\rangle$  and  $|\beta\rangle$ , can be constructed to determine component of the basis states.

$$\langle \alpha | \psi \rangle = c_1 \quad \langle \beta | \psi \rangle = c_2. \quad (1.20)$$

The outer product of the basis state,  $|r_n\rangle$ , for an N-spin system must satisfy:

$$\sum_{n=1}^N |r_n\rangle \langle r_n| = \mathbb{1}, \quad (1.21)$$

where  $\mathbb{1}$  is an N by N identity matrix.

When a second spin is introduced, the Hilbert space is extended to accommodate additional spin states by taking the tensor product of the basis states:

$$|\alpha_1 \alpha_2\rangle = |\alpha_1\rangle \otimes |\alpha_2\rangle = \begin{pmatrix} 1 \\ 0 \\ 0 \\ 0 \end{pmatrix} \quad |\alpha_1 \beta_2\rangle = |\alpha_1\rangle \otimes |\beta_2\rangle = \begin{pmatrix} 0 \\ 1 \\ 0 \\ 0 \end{pmatrix} \quad (1.22)$$

$$|\beta_1 \alpha_2\rangle = |\beta_1\rangle \otimes |\alpha_2\rangle = \begin{pmatrix} 0 \\ 0 \\ 1 \\ 0 \end{pmatrix} \quad |\beta_1 \beta_2\rangle = |\beta_1\rangle \otimes |\beta_2\rangle = \begin{pmatrix} 0 \\ 0 \\ 0 \\ 1 \end{pmatrix}. \quad (1.23)$$

The subscripts indicate which spin is being referred to, i.e.  $|\beta_1 \alpha_2\rangle$  means that spin 1 is in the  $\beta$  state and spin 2 is in the  $\alpha$  state.

### 1.2.3 Pauli matrices and more operators

In quantum mechanics each observation is associated with a particular operator. For example, the measurement of the spin angular momentum along the  $z$ -axis is associated with  $\hat{I}_z$  and when applied to the  $|\alpha\rangle$  gives the result seen in Eqn. 1.12. The probability of obtaining this result is 1 as  $|\alpha\rangle$  is an eigenstate of  $\hat{I}_z$ . In all other cases the results follow statistical laws and the result of an individual experiment is unpredictable.

In quantum mechanics there is a formula for the average result of very many observations, this is called the expectation value of a general operator,  $\hat{A}$ , when applied to a spin-1/2 system,  $|\psi\rangle$  is denoted:

$$\langle \hat{A} \rangle = \langle \psi | \hat{A} | \psi \rangle, \quad (1.24)$$

from the general case listed in Eqn. 1.16 this becomes:

$$\langle \hat{A} \rangle = \langle \psi | \hat{A} | \psi \rangle \quad (1.25)$$

$$= \begin{pmatrix} c_1^* & c_2^* \end{pmatrix} \begin{pmatrix} A_{11} & A_{12} \\ A_{21} & A_{22} \end{pmatrix} \begin{pmatrix} c_1 \\ c_2 \end{pmatrix} \quad (1.26)$$

$$= c_1 c_1^* A_{11} + c_1 c_2^* A_{12} + c_2 c_1^* A_{21} + c_2 c_2^* A_{22}. \quad (1.27)$$

The end sum of all these products is the expectation value of a single spin 1/2 particle when acted upon by  $\hat{A}$ , this quickly becomes cumbersome should there be more than one spin. An easier way to deal with expectation values is described in 1.2.4.

In NMR three operators are used to determine the projection of spin angular momentum along a specific axis,  $\hat{I}_x$ ,  $\hat{I}_y$ , and  $\hat{I}_z$ . These are defined by the Pauli matrices in the Zeeman basis multiplied by  $\hbar/2$ .

$$\hat{I}_x = \frac{\hbar}{2} \begin{pmatrix} 0 & 1 \\ 1 & 0 \end{pmatrix} \quad \hat{I}_y = \frac{\hbar}{2i} \begin{pmatrix} 0 & 1 \\ -1 & 0 \end{pmatrix} \quad \hat{I}_z = \frac{\hbar}{2} \begin{pmatrix} 1 & 0 \\ 0 & 1 \end{pmatrix}. \quad (1.28)$$

As an example, let's take a spin-1/2 particle in a magnetic field and project the  $|\alpha\rangle$  state along the  $z$ -axis.

$$\hat{I}_z |\alpha\rangle = \frac{\hbar}{2} \begin{pmatrix} 1 & 0 \\ 0 & 1 \end{pmatrix} \begin{pmatrix} 1 \\ 0 \end{pmatrix} = \frac{\hbar}{2} \begin{pmatrix} 1 \\ 0 \end{pmatrix} = \frac{\hbar}{2} |\alpha\rangle, \quad (1.29)$$

$\hbar/2$  is found to be the eigenvalue of  $|\alpha\rangle$  for the operator  $\hat{I}_z$ .

Three operators are now examined, and how they act on states is explored. They are the total square angular momentum,  $\hat{I}^2$ , and the two shift operators,  $\hat{I}^+$  and  $\hat{I}^-$ , which are defined as the following:

$$\hat{I}^2 = \hat{I}_x^2 + \hat{I}_y^2 + \hat{I}_z^2 \quad (1.30)$$

$$\hat{I}^+ = \hat{I}_x + i\hat{I}_y \quad (1.31)$$

$$\hat{I}^- = \hat{I}_x - i\hat{I}_y. \quad (1.32)$$

They act on general states according to:

$$\hat{I}^2 |I, m_I\rangle = \hbar^2 I(I+1) |I, m_I\rangle \quad (1.33)$$

$$\hat{I}^+ |I, m_I\rangle = \hbar \sqrt{(I(I+1) - m_I(m_I+1))} |I, m_{I+1}\rangle \quad (1.34)$$

$$\hat{I}^- |I, m_I\rangle = \hbar \sqrt{(I(I+1) - m_I(m_I-1))} |I, m_{I-1}\rangle. \quad (1.35)$$

Using a spin-1/2 particle in a magnetic field as an example, let these operators act on the  $|\alpha\rangle$  and  $|\beta\rangle$  states:

$$\hat{I}^2 |\alpha\rangle = \frac{3}{4} \hbar^2 |\alpha\rangle \quad (1.36)$$

$$\hat{I}^+ |\alpha\rangle = 0 \quad (1.37)$$

$$\hat{I}^- |\alpha\rangle = \hbar |\beta\rangle \quad (1.38)$$

$$\hat{I}^+ |\beta\rangle = \hbar |\alpha\rangle \quad (1.39)$$

$$\hat{I}^- |\beta\rangle = 0, \quad (1.40)$$

the '+' and '-' denote raising or lowering  $m_I$  by 1.

As shown in Eqn. 1.1, the three angular momentum operators cyclically commute. This means the *sandwich formula* applies.

In general, if  $\hat{A}$ ,  $\hat{B}$ , and  $\hat{C}$  cyclically commute, then:

$$\exp\{-i\theta\hat{A}\} \hat{B} \exp\{+i\theta\hat{A}\} = \hat{B} \cos \theta + \hat{C} \sin \theta. \quad (1.41)$$

Geometrically, this can be thought of as a rotation of  $\hat{B}$  by  $\hat{A}$  through an angle  $\theta$ .

It is important to define a set of rotation operators as these are essential for the generation of signal in NMR. They are defined as the complex exponentials of the angular momentum operators seen in 1.2.1:

$$\hat{R}_x(\theta) = \exp\{-i\theta\hat{I}_x\} \quad (1.42)$$

$$\hat{R}_y(\theta) = \exp\{-i\theta\hat{I}_y\} \quad (1.43)$$

$$\hat{R}_z(\theta) = \exp\{-i\theta\hat{I}_z\}, \quad (1.44)$$



and they too have matrix representations:

$$\hat{R}_x(\theta) = \begin{pmatrix} \cos(\frac{1}{2}\theta) & -i\sin(\frac{1}{2}\theta) \\ -i\sin(\frac{1}{2}\theta) & \cos(\frac{1}{2}\theta) \end{pmatrix} \quad (1.45)$$

$$\hat{R}_y(\theta) = \begin{pmatrix} \cos(\frac{1}{2}\theta) & \sin(\frac{1}{2}\theta) \\ \sin(\frac{1}{2}\theta) & \cos(\frac{1}{2}\theta) \end{pmatrix} \quad (1.46)$$

$$\hat{R}_z(\theta) = \begin{pmatrix} \exp\{-i\frac{1}{2}\theta\} & 0 \\ 0 & \exp\{+i\frac{1}{2}\theta\} \end{pmatrix}. \quad (1.47)$$

The rotation operators are applied to the angular momentum operators using the sandwich formula:

$$\hat{R}_x(\theta)\hat{I}_z = \exp\{-i\hat{I}_x\theta\}\hat{I}_z\exp\{+i\hat{I}_x\theta\}. \quad (1.48)$$

The result of this is a rotation of  $\hat{I}_z$  around the  $x$ -axis by an angle  $\theta$ :

$$\hat{R}_x(\theta)\hat{I}_z = \cos\theta\hat{I}_z - \sin\theta\hat{I}_y. \quad (1.49)$$

The rotational direction (sign of the  $\sin\theta$  term) is determined by the right hand co-ordinate system defined in Eqn. 1.1.

How each rotational operator transforms the spin angular momentum operators is shown below:

$$\hat{R}_x(\theta) \begin{cases} \hat{I}_x \rightarrow \hat{I}_x \\ \hat{I}_y \rightarrow \hat{I}_y \cos\theta + \hat{I}_z \sin\theta \\ \hat{I}_z \rightarrow \hat{I}_z \cos\theta - \hat{I}_y \sin\theta \end{cases} \quad (1.50)$$

$$\hat{R}_y(\theta) \begin{cases} \hat{I}_x \rightarrow \hat{I}_x \cos\theta - \hat{I}_z \sin\theta \\ \hat{I}_y \rightarrow \hat{I}_y \\ \hat{I}_z \rightarrow \hat{I}_z \cos\theta + \hat{I}_x \sin\theta \end{cases} \quad (1.51)$$

$$\hat{R}_z(\theta) \begin{cases} \hat{I}_x \rightarrow \hat{I}_x \cos\theta + \hat{I}_y \sin\theta \\ \hat{I}_y \rightarrow \hat{I}_y \cos\theta - \hat{I}_x \sin\theta \\ \hat{I}_z \rightarrow \hat{I}_z \end{cases} \quad (1.52)$$

#### 1.2.4 Density Operator

In Eqn. 1.25, the expectation value of an operator was expressed as the product of the matrix representations of the state and the operator. Simplification of this is possible by constructing a matrix of the quadratic products of the superposition coefficients. If

in the general case:

$$|\psi\rangle = \begin{pmatrix} c_1 \\ c_2 \end{pmatrix} = c_1 |\alpha\rangle + c_2 |\beta\rangle \quad (1.53)$$

$$\langle\psi| = (c_1^* \quad c_2^*) = c_1^* \langle\alpha| + c_2^* \langle\beta|, \quad (1.54)$$

then the matrix has the form:

$$|\psi\rangle \langle\psi| = \begin{pmatrix} c_1 c_1^* & c_1 c_2^* \\ c_2 c_1^* & c_2 c_2^* \end{pmatrix}. \quad (1.55)$$

The expectation value of the operator  $\hat{A}$  can now be expressed as:

$$\langle\hat{A}\rangle = \text{Tr}\{|\psi\rangle \langle\psi| \hat{A}\}. \quad (1.56)$$

If there are now  $N$  spins considered, the result of measuring  $A$  is still uncertain. However, an expression for the most likely outcome,  $A_{\text{obs}}$ , can be written by using the average of expectation values:

$$A_{\text{obs}} = \text{Tr}\{N^{-1}(|\psi_1\rangle \langle\psi_1| + |\psi_2\rangle \langle\psi_2| + \dots) \hat{A}\}. \quad (1.57)$$

this can be simplified by defining an operator,  $\hat{\rho}$ :

$$\hat{\rho} = N^{-1}(|\psi_1\rangle \langle\psi_1| + |\psi_2\rangle \langle\psi_2| + \dots), \quad (1.58)$$

where  $N$  is the number of spins in the ensemble. For brevity, this is written as:

$$\hat{\rho} = \overline{|\psi\rangle \langle\psi|}, \quad (1.59)$$

where the overbar indicates the average over all members of the ensemble.

Now the expectation of  $\hat{A}$  over all members of some spin ensemble can be written as:

$$\langle A \rangle = \text{Tr}\{\hat{\rho} \hat{A}\}, \quad (1.60)$$

the operator  $\hat{\rho}$  is referred to as the density matrix.

$$\hat{\rho} = \begin{pmatrix} \overline{c_1 c_1^*} & \overline{c_1 c_2^*} \\ \overline{c_2 c_1^*} & \overline{c_2 c_2^*} \end{pmatrix} = \begin{pmatrix} \rho_\alpha & \rho_+ \\ \rho_- & \rho_\beta \end{pmatrix}. \quad (1.61)$$

The diagonal elements of  $\hat{\rho}$ ,  $\rho_\alpha$  and  $\rho_\beta$ , are state populations or the probabilities of being in a certain state.

The off-diagonal elements are coherences between states. These coherences represent superposition states in the ensemble, the coherences are complex numbers and two coherences between the same pair of states are complex conjugates of each other i.e.:

$$\langle \alpha | \hat{\rho} | \beta \rangle = (\langle \beta | \hat{\rho} | \alpha \rangle)^* = c_1 c_2^* = (c_1^* c_2)^*. \quad (1.62)$$

The coherence order between two states in a magnetic field is defined as the difference in spin angular momentum projection along the  $z$  axis. In our two spin system this would be:

$$\hat{I}_z |\alpha\rangle = m_\alpha = +\frac{1}{2}\hbar |\alpha\rangle \quad (1.63)$$

$$\hat{I}_z |\beta\rangle = m_\beta = -\frac{1}{2}\hbar |\beta\rangle. \quad (1.64)$$

These results can be used to calculate the coherence order of the coherence  $\rho_+$ :

$$m_\alpha - m_\beta = +1, \quad (1.65)$$

and conversely the coherence order of  $\rho_-$  is:

$$m_\beta - m_\alpha = -1. \quad (1.66)$$

The density operator can be written as:

$$\hat{\rho} = \rho_\alpha \hat{I}^\alpha + \rho_\beta \hat{I}^\beta + \rho_+ \hat{I}^+ + \rho_- \hat{I}^-, \quad (1.67)$$

using the shift operators,  $\hat{I}^+$  and  $\hat{I}^-$ , and the projection operators,  $\hat{I}^\alpha$  and  $\hat{I}^\beta$ , these have the following matrix representations:

$$\begin{aligned} \hat{I}^+ &= \hbar \begin{pmatrix} 0 & 1 \\ 0 & 0 \end{pmatrix} & \hat{I}^- &= \hbar \begin{pmatrix} 0 & 0 \\ 1 & 0 \end{pmatrix} \\ \hat{I}^\alpha &= \frac{\hbar}{2} \begin{pmatrix} 1 & 0 \\ 0 & 0 \end{pmatrix} & \hat{I}^\beta &= \frac{\hbar}{2} \begin{pmatrix} 0 & 0 \\ 0 & 1 \end{pmatrix}. \end{aligned}$$

The physical interpretations of the components of the density operator can help to understand the microscopic state of the individual spins. The sum of the populations,  $\rho_\alpha$  and  $\rho_\beta$ , is always equal to one, only the differences between the states have any significance. The difference in population indicates the net longitudinal spin polarization, i.e. if the  $|\alpha\rangle$  state population is larger than the  $|\beta\rangle$  state, then there is net polarization of the spins along the external field direction.

The presence of the coherences,  $\rho_+$  and  $\rho_-$ , indicates transverse spin magnetization i.e. net spin polarization *perpendicular* to the external field. These coherences are

complex numbers and as such have phase and amplitude. The phase of the coherences indicates the direction of the spin polarization in the  $xy$ -plane. The  $(-1)$ -quantum coherence is written as:

$$\rho_- = |\rho_-| \exp\{i\phi_-\}, \quad (1.68)$$

and the polarization axis of the spins is:

$$\mathbf{e}'_x \cos \phi_- + \mathbf{e}'_y \sin \phi_-. \quad (1.69)$$

These populations and coherences play a vital role in NMR and will be re-visited in a later section.

### 1.2.5 The Hamiltonian

The Hamiltonian plays an important part in quantum systems. When the Hamiltonian acts on an eigenstate, the eigenvalue returned is the energy level of that state.

#### 1.2.5.1 Spins in a magnetic field

In NMR the energy of a nucleus in a magnetic field,  $E$ , is given by:

$$E = -m_I \hbar \gamma B_0, \quad (1.70)$$

where  $m_I$  is the azimuthal quantum number,  $\hbar$  is the reduced Planck constant,  $\gamma$  is the gyromagnetic ratio, and  $B_0$  is the external field taken to be orientated along the  $z$ -axis.

For a spin-1/2 nuclei there are two states labelled as  $\alpha$  and  $\beta$  and these have an energy difference depicted in Fig. 1.5.

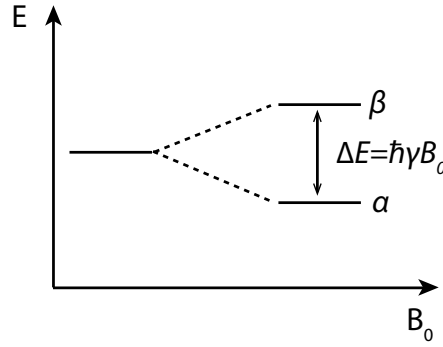


FIGURE 1.5: Energy level and  $\Delta E$  of the two energy levels for a spin-1/2 nucleus.

This splitting of energy levels due to the presence of a magnetic field is referred to as Zeeman splitting. When examining a spin ensemble at thermal equilibrium, overall, there is a slight bias to the lower energy state  $\alpha$ . This preference can be quantified by calculating the ratio of the populations:

$$\frac{\rho_\beta}{\rho_\alpha} = \exp\left\{\frac{-\Delta E}{k_B T}\right\}, \quad (1.71)$$

where  $\rho_\beta/\rho_\alpha$  is the population ratio between the states,  $k_B$  is the Boltzmann constant, and  $T$  is the temperature. The polarization,  $p$ , of a system of spin-1/2 nuclei is

$$p = \frac{\rho_\alpha - \rho_\beta}{\rho_\alpha + \rho_\beta} = \tanh\left(\frac{\gamma \hbar B_0}{2k_B T}\right). \quad (1.72)$$

For a typical NMR experiment, which operates at  $298K$  and a field of  $14.1\text{ T}$ , the polarization level,  $p \approx 10^{-5}$  which means that the spins are aligned weakly in the same direction as the magnetic field. It is this small polarization that gives rise to the NMR signal. One possible solution to the low polarization levels at thermal equilibrium is called hyperpolarization, and involves strategies that produce non equilibrium polarization levels.

When placed in a magnetic field, the nuclei will precess around the axis of the field at a rate known as the Larmor frequency, this is defined as:

$$\omega_j^0 = -\gamma_j B_0, \quad (1.73)$$

where  $\gamma_j$  is the gyromagnetic ratio for a nucleus,  $j$ . The gyromagnetic ratio is typically 10s of  $\text{MHz T}^{-1}$  which give Larmor frequencies in the 100s of  $\text{MHz}$  in an NMR experiment.

If  $|\psi_1\rangle$  and  $|\psi_2\rangle$  are eigenstates of the Hamiltonian  $\hat{\mathcal{H}}$ , then

$$\hat{\mathcal{H}} |\psi_1\rangle = E_1 |\psi_1\rangle \quad (1.74)$$

$$\hat{\mathcal{H}} |\psi_2\rangle = E_2 |\psi_2\rangle. \quad (1.75)$$

The Hamiltonian can also be expressed in matrix form:

$$\hat{\mathcal{H}} = \begin{pmatrix} E_1 & 0 \\ 0 & E_2 \end{pmatrix}. \quad (1.76)$$

If the Hamiltonian is written in the eigenbasis of the system, its main diagonal corresponds to state energies and it has values of 0 everywhere else.

The evolution in time of a quantum system is described by the Schrödinger equation:

$$\frac{d}{dt} |\psi\rangle = i\hbar^{-1} \hat{\mathcal{H}} |\psi\rangle. \quad (1.77)$$

The factor of  $\hbar^{-1}$  here is cumbersome and can be removed by defining a Hamiltonian in natural units,  $\hat{H}$ , such that:

$$\hat{H} = \hbar^{-1} \hat{\mathcal{H}}. \quad (1.78)$$

Both of these Hamiltonians share the same eigenfunctions:

$$\hat{H} |\psi_1\rangle = \omega_{\psi_1} |\psi_1\rangle, \quad (1.79)$$

the eigenvalues are denoted  $\omega_{\psi}$  and are given by:

$$\omega_{\psi_1} = \hbar^{-1} E_1, \quad (1.80)$$

and the eigenvalue,  $\omega_{\psi_1}$ , is the energy of the state  $|\psi\rangle$  in *units* of  $\hbar$ .

Returning to the example of a spin-1/2 particle in a magnetic field, the Hamiltonian is initially proportional to the  $z$  angular momentum operator:

$$\hat{H} = \omega^0 \hat{I}_z, \quad (1.81)$$

where  $\omega^0 = -\gamma B_0$  and is the Larmor frequency from Eqn. 1.73. In matrix form, in the original Zeeman basis, the Hamiltonian is:

$$\hat{H} = \begin{pmatrix} +\frac{\omega}{2} & 0 \\ 0 & -\frac{\omega}{2} \end{pmatrix}, \quad (1.82)$$

where

$$\hat{H} |\alpha\rangle = +\frac{\omega}{2} |\alpha\rangle. \quad (1.83)$$

### 1.2.6 Spin precession

As discussed when describing Larmor frequency when a spin-1/2 particle is placed in a magnetic field it precesses at the Larmor frequency. In quantum mechanics this precession means that the spin state  $|\psi\rangle$  depends on time.

The law of motion for the spin is the time dependent Schrödinger equation:

$$\frac{d}{dt} |\psi\rangle(t) = -i\hat{H} |\psi\rangle(t). \quad (1.84)$$

The spin Hamiltonian is:

$$\hat{H} = \omega^0 \hat{I}_z, \quad (1.85)$$

the equation of motion then becomes:

$$\frac{d}{dt} |\psi\rangle(t) = -i\omega^0 \hat{I}_z |\psi\rangle(t), \quad (1.86)$$

this is a first order differential equation that has the solution:

$$|\psi\rangle(t) = \exp\{-i\omega^0 \Delta t \hat{I}_z\} \psi(t_0), \quad (1.87)$$

where  $t_0$  is the initial time and  $\Delta t$  is the difference in time between  $t_0$  and  $t$ . As the  $\omega^0 \Delta t$  term is angular frequency multiplied by time this simply gives an angle. This shows that it is equal to a rotation about the  $z$ -axis:

$$\hat{R}_z \theta = \exp\{-i\theta \hat{I}_z\}. \quad (1.88)$$

The solution therefore to the Schrödinger equation in the absence of r.f. fields is:

$$|\psi\rangle(t) = \hat{R}_z(\omega^0 \Delta t) |\psi\rangle(t_0). \quad (1.89)$$

In the absence of r.f. fields the Schrödinger equation says that the spin rotates around the  $z$ -axis, through the angle  $\omega_0 \Delta t$

### 1.2.7 Rotating Frame

The field,  $B_0$ , of a regular NMR experiment is many Tesla, giving precession frequencies of hundreds of megahertz. These frequencies correspond to radio frequencies in the electromagnetic spectrum. When considering these precessing spins it can be useful to change from a static frame to a rotating frame of reference.

the static frame of reference axes ( $x$ ,  $y$ , and  $z$ ) and the rotating frame axes ( $x'$ ,  $y'$ , and  $z'$ ) of reference are connected through a time dependent angle,  $\Phi(t)$  such that:

$$x' = x \cos \Phi(t) + y \sin \Phi(t) \quad (1.90)$$

$$y' = y \cos \Phi(t) - x \sin \Phi(t) \quad (1.91)$$

$$z' = z. \quad (1.92)$$

The frame rotates with a constant frequency  $\omega_{\text{ref}}$  around the  $z$ -axis:

$$\Phi(t) = \omega_{\text{ref}} t + \phi_{\text{ref}}, \quad (1.93)$$

for brevity ( $t$ ) is now dropped.

If a spin in state  $|\psi\rangle$  has a Larmor frequency equal to  $\omega_{\text{ref}}$  then the spin state in the rotating frame,  $|\tilde{\psi}\rangle$  is:

$$|\tilde{\psi}\rangle = \hat{R}_z(-\Phi) |\psi\rangle, \quad (1.94)$$

where the tilde denotes a state in the rotating frame.

These of course have an equation of motion:

$$\frac{d}{dt} |\tilde{\psi}\rangle = i\hbar^{-1} \hat{\tilde{H}} |\tilde{\psi}\rangle, \quad (1.95)$$

where:

$$\hat{\tilde{H}} = \hat{R}_z(-\Phi) \hat{H} \hat{R}_z(\Phi) - \omega_{\text{ref}} \hat{I}_z. \quad (1.96)$$



### 1.2.7.1 Precession in the rotating frame

The spin Hamiltonian in a static field is:

$$\hat{H}^0 = \omega^0 \hat{I}_z. \quad (1.97)$$

The rotating frame Hamiltonian is:

$$\hat{\tilde{H}} = \omega^0 \hat{R}_z(-\Phi) \hat{I}_z \hat{R}_z(\Phi) - \omega_{\text{ref}} \hat{I}_z = (\omega^0 - \omega_{\text{ref}}) \hat{I}_z. \quad (1.98)$$

The frequency  $\omega^0 - \omega_{\text{ref}}$  is the difference between the Larmor frequency and that of the frame and is denoted,  $\Omega^0$ :

$$\Omega^0 = \omega^0 - \omega_{\text{ref}}. \quad (1.99)$$

The rotating-frame spin Hamiltonian in the presence of a static field, is therefore:

$$\hat{\tilde{H}} = \Omega^0 \hat{I}_z. \quad (1.100)$$

## 1.2.8 Radio Frequency Pulses

In NMR 'pulses' are used to manipulate the spin states. These pulses take the form of an oscillating magnetic field applied at a frequency such that it is resonant with the precessing spin. The frequencies correspond to radio frequencies and as such, the pulses and fields are referred to as r.f. pulses and r.f. fields respectively.

When an r.f. pulse is applied, the spin experiences two magnetic fields: a static field generated by the magnet; and an oscillating field from the excitation coil. The static field is much larger than the oscillating r.f. field.

The weak r.f. field produces a large effect on the nuclear spin due to it being *resonant* with the precession of that spin. This allows the effect of the weak r.f. field to accumulate as time goes on. If the pulse is applied for long enough, then the weak r.f. field can cause a large change in the spin state. In practice, this corresponds to applying several microseconds of an r.f. pulse, which allows for several hundred Larmor precession cycles.

For an r.f. pulse of general phase,  $\phi_p$ , the r.f. field oscillates at the spectrometer resonance frequency,  $\omega_{\text{ref}}$ , and the spin Hamiltonian during the r.f. pulse is given by:

$$\hat{H} = \omega^0 \hat{I}_z + \hat{H}_{\text{RF}} t, \quad (1.101)$$

where

$$\hat{H}_{\text{RF}}(t) = -\frac{1}{2} \gamma B_{\text{RF}} \sin \theta_{\text{RF}} \hat{R}_z(\Phi_p) \hat{I}_x \hat{R}_z(-\Phi_p), \quad (1.102)$$

where  $\theta_{\text{RF}}$  is the angle between the RF coil and the sample, and

$$\Phi_p(t) = \omega_{\text{ref}}t + \phi_p. \quad (1.103)$$

The rotating frame Hamiltonian is:

$$\hat{\tilde{H}} = -\frac{1}{2}\gamma B_{\text{RF}} \sin \theta_{\text{RF}} \hat{R}_z(-\Phi + \Phi_p) \hat{I}_x \hat{R}_z(\Phi - \Phi_p) + (\omega^0 - \omega_{\text{ref}}) \hat{I}_z \quad (1.104)$$

$$= -\frac{1}{2}\gamma B_{\text{RF}} \sin \theta_{\text{RF}} \hat{R}_z(-\phi_{\text{ref}} + \phi_p) \hat{I}_x \hat{R}_z(\phi_{\text{ref}} - \phi_p) + \Omega^0 \hat{I}_z, \quad (1.105)$$

an additional simplification is possible if the value of  $\phi_{\text{ref}}$ , which is  $\pi$  for positive  $\gamma$  spins, and has the effect of changing the sign of the  $\gamma B_{\text{RF}}$  term is included:

$$\hat{\tilde{H}} = \omega_{\text{nut}} \hat{R}_z(\phi_p) \hat{I}_x \hat{R}_z(-\phi_p) + \Omega^0 \hat{I}_z, \quad (1.106)$$

where  $\omega_{\text{nut}}$  is the nutation frequency:

$$\omega_{\text{nut}} = |-\frac{1}{2}\gamma B_{\text{RF}} \sin \theta_{\text{RF}}|, \quad (1.107)$$

the nutation frequency is the measure of the r.f. field amplitude.

Using the sandwich property again the final form of the rotating-frame Hamiltonian during an r.f. pulse is:

$$\hat{\tilde{H}} = \Omega^0 \hat{I}_z + \omega_{\text{nut}} (\hat{I}_x \cos \phi_p + \hat{I}_y \sin \phi_p). \quad (1.108)$$

### 1.2.8.1 $x$ -pulse

To illustrate the effect an r.f. pulse has on a sample, consider a strong pulse with frequency  $\omega_{\text{ref}}$ , duration  $\tau$ , and phase  $\phi_p = 0$  (an ' $x$ -pulse'). The amplitude is given by  $\omega_{\text{ref}}$ . Assuming this pulse to be applied directly on resonance such that  $\Omega^0 = 0$ . The rotating frame spin Hamiltonian is:

$$\hat{\tilde{H}} = \omega_{\text{nut}} \hat{I}_x, \quad (1.109)$$

the motion of the spin states may be found using the rotating frame Schrödinger equation. If the spin state before the pulse is given by  $|\tilde{\psi}\rangle_1$  and the spin state after the pulse is  $|\tilde{\psi}\rangle_2$  then they are related by:

$$|\tilde{\psi}\rangle_2 = \hat{R}_x(\theta) |\tilde{\psi}\rangle_1, \quad (1.110)$$

where the rotation operator is as defined in Eqn. 1.42 and the angle  $\theta$  is given by

$$\theta = \omega_{\text{nut}} \tau, \quad (1.111)$$

this angle is referred to as the *flip angle* of the pulse.

To calculate what effect the pulse has on spins in specific states the matrix representation can be used. A  $(\pi/2)_x$  pulse, which means a flip angle of  $\theta = \pi/2$  and a phase of  $\phi_p = 0$ , applied to spin in the state  $|\alpha\rangle$  can be calculated using the matrix representation of  $\hat{R}_x(\theta)$  as:

$$\hat{R}_x(\pi/2)|\alpha\rangle = \frac{1}{\sqrt{2}} \begin{pmatrix} \cos(\frac{1}{2}\pi/2) & -i\sin(\frac{1}{2}\pi/2) \\ -i\sin(\frac{1}{2}\pi/2) & \cos(\frac{1}{2}\pi/2) \end{pmatrix} \begin{pmatrix} 1 \\ 0 \end{pmatrix} \quad (1.112)$$

$$= \frac{1}{\sqrt{2}} \begin{pmatrix} 1 & -i \\ -i & 1 \end{pmatrix} \begin{pmatrix} 1 \\ 0 \end{pmatrix} \quad (1.113)$$

$$= \frac{1}{\sqrt{2}} \begin{pmatrix} 1 \\ -i \end{pmatrix} = e^{-i\pi/4} \frac{1}{2} \begin{pmatrix} 1+i \\ 1-i \end{pmatrix} = e^{i\pi/4} | -y \rangle. \quad (1.114)$$

The pulse transforms the state  $|\alpha\rangle$  into the state  $| -y \rangle$  in other words it has rotated the polarization by  $\pi/2$  around the  $x$ -axis.

### 1.2.8.2 Pulse of general phase

To understand the significance of the phase of a pulse, consider a pulse exactly on resonance ( $\Omega^0 = 0$ ) with a general phase  $\phi_p$ . The rotating frame spin Hamiltonian is:

$$\hat{H} = \omega_{\text{nut}} (\hat{I}_x \cos \phi_p + \hat{I}_y \sin \phi_p), \quad (1.115)$$

from this, one can see that the effect of the phase shift is to change the axis about which the spin polarizations rotate. The rotation axis is still in the  $xy$ -plane but forms an angle,  $\phi_p$ , with the  $x$  axis. Therefore, a pulse with a phase of  $\pi/2$  rotates the spin polarization around the  $y$ -axis and a phase of  $\pi$  rotates the polarization around the  $-x$ -axis and so on.

The propagator for an on resonance pulse with phase  $\phi_p$  is given by:

$$\hat{R}_{\phi_p}(\theta) = \exp\{-i\omega_{\text{nut}}\tau(\hat{I}_x \cos \phi_p + \hat{I}_y \sin \phi_p)\} \quad (1.116)$$

$$= \exp\{-i\theta(\hat{I}_x \cos \phi_p + \hat{I}_y \sin \phi_p)\}, \quad (1.117)$$

this can be rewritten using rotation operators:

$$\hat{R}_{\phi_p}(\theta) = \hat{R}_z(\phi_p) \hat{R}_x(\theta) \hat{R}_z(-\phi_p). \quad (1.118)$$

The matrix representation can be obtained by multiplying together the matrix representations of the rotation operators from Eqn. 1.45:

$$\hat{R}_{\phi_p}(\theta) = \begin{pmatrix} \cos \frac{1}{2}\theta & -i \sin \frac{1}{2}(\theta)e^{-i\phi_p} \\ -i \sin \frac{1}{2}(\theta)e^{+i\phi_p} & \cos \frac{1}{2}\theta \end{pmatrix}. \quad (1.119)$$

### 1.2.8.3 Off-resonance effects

In general, it is not always possible to ensure exact resonance for all spins at the same time, so the condition  $\Omega^0 = 0$  cannot always be satisfied. Consider the case when  $\Omega^0 \neq 0$ , by examining the spin Hamiltonian during a rectangular pulse where:

$$\hat{\tilde{H}} = \Omega^0 \hat{I}_z + \omega_{\text{nut}}(\hat{I}_x \cos \phi_p + \hat{I}_y \sin \phi_p). \quad (1.120)$$

The rotation axis of the spin polarization now has a  $z$ -component as well as an  $x$ - and  $y$ -component. The axis is therefore tilted out of the  $xy$ -plane.

The rotating frame spin Hamiltonian for an off-resonance pulse may be written as:

$$\hat{\tilde{H}} = \omega_{\text{eff}} \cdot \hat{\mathbf{I}}, \quad (1.121)$$

where  $\omega_{\text{eff}}$  is the effective rotation axis, given by:

$$\omega_{\text{eff}} = \omega_{\text{eff}}\{\mathbf{e}'_x \sin \beta_p \cos \phi_p + \mathbf{e}'_y \sin \beta_p \sin \phi_p + \mathbf{e}'_z \cos \beta_p\}, \quad (1.122)$$

and  $\{\mathbf{e}'_x, \mathbf{e}'_y, \mathbf{e}'_z\}$  are the rotating reference frame axes. The vector operator  $\hat{\mathbf{I}}$  is defined as:

$$\hat{\mathbf{I}} = \mathbf{e}'_x \hat{I}_x + \mathbf{e}'_y \hat{I}_y + \mathbf{e}'_z \hat{I}_z. \quad (1.123)$$

The tilt of the rotation axis away from the  $z$ -axis is:

$$\beta_p = \arctan\left(\frac{\omega_{\text{nut}}}{\Omega^0}\right), \quad (1.124)$$

the magnitude of the rotation frequency around the tilted axis is given by:

$$\omega_{\text{eff}} = \{(\omega_{\text{nut}})^2 + (\Omega^0)^2\}^{1/2}, \quad (1.125)$$

Using these parameters the rotating frame spin Hamiltonian may be written as:

$$\hat{\tilde{H}} = \omega_{\text{eff}} \hat{R}_z(\phi_p) \hat{R}_y(\beta_p) \hat{I}_z \hat{R}_y(-\beta_p) \hat{R}_z(-\phi_p). \quad (1.126)$$

The rotating-frame spin states before and after the pulse are related through:

$$|\tilde{\psi}\rangle_2 = \hat{R}_{\text{off}} |\tilde{\psi}\rangle_1, \quad (1.127)$$

where  $\hat{R}_{\text{off}}$  is:

$$\hat{R}_{\text{off}} = \hat{R}_z(\phi_p) \hat{R}_y(\beta_p) \hat{R}_z(\omega_{\text{eff}}\tau) \hat{R}_y(-\beta_p) \hat{R}_z(-\phi_p). \quad (1.128)$$

### 1.2.9 The Density operator revisited

Usually in NMR there are  $> 10^{20}$  spins in the sample, the density operator becomes more advantageous here as mentioned it contains information about the entire spin ensemble. Normally, there is only a small population difference between  $\alpha$  and  $\beta$  governed by the Boltzmann distribution, so for a general polarization level,  $p$ , the density operator can be written as:

$$\hat{\rho} = \frac{1}{2} \begin{pmatrix} 1+p & 0 \\ 0 & 1-p \end{pmatrix}, \quad (1.129)$$

using the definition given in Eqn. 1.29 the density operator can be re-written as

$$\hat{\rho} = \frac{1}{2} \hat{\mathbb{1}} + \frac{1}{2} p \hat{I}_z, \quad (1.130)$$

$\hat{\mathbb{1}}$  is identity matrix defined as:

$$\hat{\mathbb{1}} = \begin{pmatrix} 1 & 0 \\ 0 & 1 \end{pmatrix}, \quad (1.131)$$

and corresponds to no population difference between  $|\alpha\rangle$  and  $|\beta\rangle$ .

$\hat{\mathbb{1}}$  is unaffected by rotations so can be ignored in the context of NMR and it becomes

$$\hat{\rho} = \frac{1}{2} p \hat{I}_z, \quad (1.132)$$

to describe the  $z$  magnetization of our sample. If the system is at thermal equilibrium, then  $p$  is equal to the Boltzmann factor defined as:

$$\mathbb{B} = \frac{\hbar\gamma B_0}{k_b T}. \quad (1.133)$$

In NMR the dynamics of a system can be described using the density operator evolution, rather than the evolution of the states using

$$\frac{\partial}{\partial t} |\psi\rangle = -i\hat{H} |\psi\rangle \quad (1.134)$$

$$\frac{\partial}{\partial t} \langle\psi| = i \langle\psi| \hat{H}, \quad (1.135)$$

Using this, the following derivation can be made [80]:

$$\frac{\partial}{\partial t} \hat{\rho} = \frac{\partial}{\partial t} [|\psi\rangle \langle\psi|] \quad (1.136)$$

$$= \left[ \frac{\partial}{\partial t} |\psi\rangle \right] \langle\psi| + |\psi\rangle \left[ \frac{\partial}{\partial t} \langle\psi| \right] \quad (1.137)$$

$$= -i\hat{H} |\psi\rangle \langle\psi| + i |\psi\rangle \langle\psi| \hat{H}, \quad (1.138)$$

to give the relationship

$$\frac{\partial}{\partial t} \hat{\rho} = -i[\hat{H}, \hat{\rho}]. \quad (1.139)$$

This is called the Liouville von Neumann equation.

The calculation of the response of the spin ensemble to r.f. pulses can be done, given the general rotating frame as before, the rotating frame density operator is given by:

$$\hat{\tilde{\rho}} = \overline{|\tilde{\psi}\rangle \langle\tilde{\psi}|}. \quad (1.140)$$

The rotating frame and fixed frame populations and coherences are related by:

$$\tilde{\rho}_{\alpha} = \rho_{\alpha} \quad \tilde{\rho}_{\beta} = \rho_{\beta} \quad (1.141)$$

$$\tilde{\rho}_{-} = \rho_{-} \exp\{-i\Phi(t)\} \quad \tilde{\rho}_{+} = \rho_{+} \exp\{+i\Phi(t)\}, \quad (1.142)$$

where

$$\Phi(t) = \omega_{\text{ref}} t + \phi_{\text{ref}}, \quad (1.143)$$

the populations remain the same and the coherences are linked through a time dependant phase factor.

### 1.2.9.1 Magnetization vector

The state of a single spin-1/2 can be represented by an arrow indicating the direction of well-defined angular momentum and the response measured by rotating the arrow around the different axes in three dimensional space. Then similarly an ensemble of isolated spins-1/2 can be represented as a magnetization vector,  $\mathbf{M}$ , indicating the magnitude and direction of the net magnetization. The dynamics of the ensemble corresponds to the motion of the magnetization vector.

The magnetization vector has three Cartesian components:

$$\mathbf{M} = M_x \mathbf{e}_x + M_y \mathbf{e}_y + M_z \mathbf{e}_z. \quad (1.144)$$

The longitudinal component is related to the population difference between states:

$$M_z = 2\mathbb{B}^{-1}(\rho_{\alpha} - \rho_{\beta}). \quad (1.145)$$

The transverse magnetization components  $M_x$  and  $M_y$  are related to the  $(-1)$ -quantum coherence between the states:

$$M_x = 4\mathbb{B}^{-1} \text{Re}\{\rho_{-}\} \quad (1.146)$$

$$M_y = 4\mathbb{B}^{-1} \text{Im}\{\rho_{-}\}. \quad (1.147)$$

These are chosen so that thermal equilibrium magnetization is a unit vector along the  $z$ -axis:

$$\mathbf{M}^{\text{eq}} = \mathbf{e}_z. \quad (1.148)$$

With these, the density operator may be written as:

$$\hat{\rho} = \frac{1}{2}\mathbb{1} + \frac{1}{2}\mathbb{B}\mathbf{M} \cdot \hat{\mathbf{I}} \quad (1.149)$$

$$= \frac{1}{2}\mathbb{1} + \frac{1}{2}\mathbb{B}(M_x \hat{I}_x + M_y \hat{I}_y + M_z \hat{I}_z). \quad (1.150)$$

The populations and coherences can be represented in terms of magnetization:

$$\rho_{\alpha} = \frac{1}{2} + \frac{1}{4}\mathbb{B}M_z \quad \rho_{\beta} = \frac{1}{2} - \frac{1}{4}\mathbb{B}M_z \quad (1.151)$$

$$\rho_{+} = \frac{1}{4}\mathbb{B}(M_x - iM_y) \quad \rho_{-} = \frac{1}{4}\mathbb{B}(M_x + iM_y). \quad (1.152)$$

### 1.2.9.2 Density operator under pulses

The sandwich equation can be used to calculate the effect of a strong  $(\pi/2)_x$  pulse on an ensemble of spins-1/2 at thermal equilibrium. Before the pulse, the spin density operator is

$$\hat{\rho}_1 = \frac{1}{2}\mathbb{1} + \frac{1}{2}\mathbb{B}\hat{I}_z, \quad (1.153)$$

after the pulse the density operator is

$$\hat{\rho}_2 = \hat{R}_x(\pi/2)\hat{\rho}_1\hat{R}_x(-\pi/2) = \frac{1}{2}\hat{R}_x(\pi/2)\mathbb{1}\hat{R}_x(-\pi/2) + \frac{1}{2}\mathbb{B}\hat{R}_x(\pi/2)\hat{I}_z\hat{R}_x(-\pi/2) \quad (1.154)$$

$$= \frac{1}{2}\mathbb{1} + \frac{1}{2}\mathbb{B}\hat{R}_x(\pi/2)\hat{I}_z\hat{R}_x(-\pi/2), \quad (1.155)$$

since the identity matrix,  $\mathbb{1}$  is invariant under rotations. The last term can be calculated using the sandwich relationship:

$$\hat{R}_x(\pi/2)\hat{I}_z\hat{R}_x(-\pi/2) = -\hat{I}_y, \quad (1.156)$$

therefore

$$\hat{\rho}_2 = \frac{1}{2}\mathbb{1} - \frac{1}{2}\mathbb{B}\hat{I}_y. \quad (1.157)$$

In terms of the magnetization vector, this is equivalent to rotating the magnetization from the  $z$ -axis to the  $-y$ -axis.

$$\mathbf{M}_1 = \mathbf{e}_z \xrightarrow{(\pi/2)_x} \mathbf{M}_2 = -\mathbf{e}_y. \quad (1.158)$$

To determine what happens to the populations and coherences, consider the pulse effects in terms of the matrix representation:

$$\hat{\rho}_1 = \begin{pmatrix} \frac{1}{2} + \frac{1}{4}\mathbb{B} & 0 \\ 0 & \frac{1}{2} - \frac{1}{4}\mathbb{B} \end{pmatrix} \xrightarrow{(\pi/2)_x} \begin{pmatrix} \frac{1}{2} & -\frac{1}{4i}\mathbb{B} \\ \frac{1}{4i}\mathbb{B} & \frac{1}{2} \end{pmatrix}, \quad (1.159)$$

the pulse accomplishes two things, firstly, the pulse equalises the populations of the two states and secondly, converts the population difference into coherences.

### 1.2.10 Free evolution with relaxation

So far, the Hamiltonian and density operator have only been discussed before, during, and immediately after an r.f. pulse. This picture is insufficient to describe what one observes experimentally. In terms of populations and coherences, experimentally it is found that the populations are not time independent, but gradually drift towards their thermal equilibrium values and that the coherences do not last forever but gradually decay to zero.

For populations and coherences there are two forms of relaxation,  $T_1$  and  $T_2$ .  $T_1$  is the longitudinal relaxation time constant and  $T_2$  is the transverse relaxation time constant. The difference between them is demonstrated in Fig. 1.6. Classically  $T_1$  is the rate constant that governs the return of magnetization to the  $z$ -axis from the  $xy$ -plane.  $T_2$  on the other hand is the time constant that governs the return of magnetization to equilibrium in the  $xy$ -plane. When talking in terms of the density operator it is said that ' $T_1$ ' is the relaxation rate constant for populations, and ' $T_2$ ' is the relaxation rate constant coherences. But this is incompatible with the classical description of NMR.

The Bloch equations are used to describe how the magnetization vectors change in time [81]:

$$\frac{dM_x(t)}{dt} = \gamma(M_y(t)B_z(t) - M_z(t)B_y(t)) - \frac{M_x(t)}{T_2} \quad (1.160)$$

$$\frac{dM_y(t)}{dt} = \gamma(M_z(t)B_x(t) - M_x(t)B_z(t)) - \frac{M_y(t)}{T_2} \quad (1.161)$$

$$\frac{dM_z(t)}{dt} = \gamma(M_x(t)B_y(t) - M_y(t)B_x(t)) - \frac{M_z(t) - M_0}{T_1}. \quad (1.162)$$



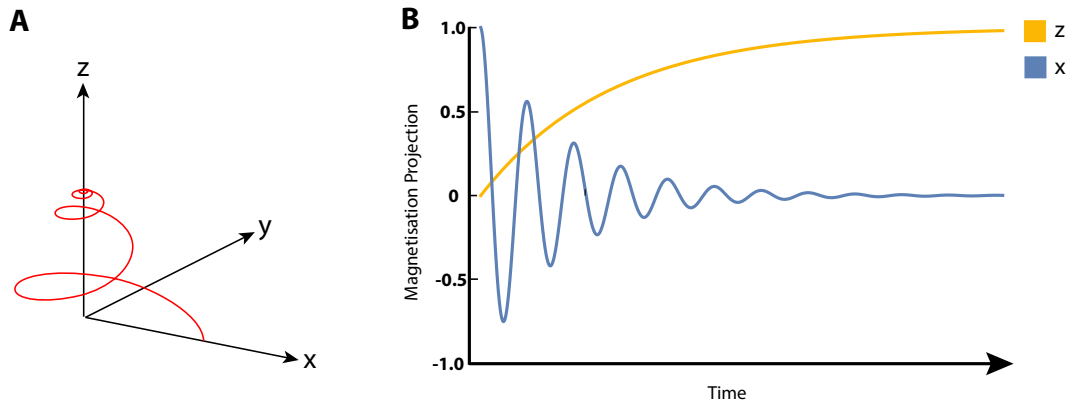


FIGURE 1.6: A) a magnetization vector precesses in the  $xy$ -plane, eventually returning to equilibrium. B) A plot of the magnetization along  $z$ -axis (yellow) and the  $x$ -axis (blue) during the relaxation.

### 1.2.10.1 Transverse relaxation

The coherences decaying to zero is ensured in the equations by introducing an exponential decay term. between time points 2, immediately after an r.f. pulse ( $t=0$ ), and 3 ( $t>0$ ) with some delay  $\tau$  the equations for the rotating frame coherences are:

$$\rho_{-}(3) = \rho_{-}(2)\exp\{(i\Omega^0 - \lambda)\tau\} \quad (1.163)$$

$$\rho_{+}(3) = \rho_{+}(2)\exp\{(-i\Omega^0 - \lambda)\tau\}, \quad (1.164)$$

where the damping rate constant  $\lambda$  is given by the inverse of the transverse relaxation time constant  $T_2$ :

$$\lambda = T_2^{-1}. \quad (1.165)$$

These equations for coherences correspond to the following substitution rules for the transverse spin angular momentum operators:

$$\hat{I}_x \rightarrow (\hat{I}_x \cos \Omega^0 \tau + \hat{I}_y \sin \Omega^0 \tau)e^{-\lambda \tau} \quad (1.166)$$

$$\hat{I}_y \rightarrow (\hat{I}_y \cos \Omega^0 \tau - \hat{I}_x \sin \Omega^0 \tau)e^{-\lambda \tau}. \quad (1.167)$$

For the transverse components of the magnetization vector, the equations are:

$$M_x(3) = M_x(2) \cos \Omega^0 \tau + M_y(2) \sin \Omega^0 \tau e^{-\lambda \tau} \quad (1.168)$$

$$M_y(3) = M_y(2) \cos \Omega^0 \tau - M_x(2) \sin \Omega^0 \tau e^{-\lambda \tau}. \quad (1.169)$$

Physically, coherence requires a consistent polarization direction of the spin ensemble. On average all spins experience the same field in a liquid due to motional

averaging, however, at any particular instant in time the field are slightly different for different spins locally which cause a gradual loss of synchronisation across the ensemble. Coherence decay does increase the entropy of the spin ensemble and is therefore irreversible.

### 1.2.10.2 Longitudinal relaxation

The equations of motion for the populations is a bit more complicated as the populations decay back to their thermal equilibrium values the equations for this are:

$$\rho_\alpha(3) = (\rho_\alpha(2) - \rho_\alpha^{eq})e^{-\tau/T_1} + \rho_\alpha^{eq} \quad (1.170)$$

$$\rho_\beta(3) = (\rho_\beta(2) - \rho_\beta^{eq})e^{-\tau/T_1} + \rho_\beta^{eq}, \quad (1.171)$$

where the thermal equilibrium populations are:

$$\rho_\alpha^{eq} = \frac{1}{2} + \frac{1}{4}\mathbb{B} \quad \rho_\beta^{eq} = \frac{1}{2} - \frac{1}{4}\mathbb{B}. \quad (1.172)$$

The equation of motion for the  $z$ -axis magnetization vector is:

$$M_z(3) = (M_z(2) - 1)e^{-\tau/T_1} + 1. \quad (1.173)$$

Longitudinal relaxation involves an energy exchange between the spin system and the molecular surroundings and is why it is often referred to as spin-lattice relaxation.

### 1.2.11 NMR signal and detection

In NMR the signal produced by the spins is inductively detected. The precessing transverse magnetization, created when an r.f. field is applied to the sample, induces a voltage, and therefore a current, in a coil that is placed near the sample.

In order to do this, consider a sample containing  $n_s$  number of non-interacting spins-1/2 which have a sample volume,  $V_s$ , and a concentration of spins,  $c_s = n_s/V_s$ . The total magnetic dipole moment operator in this case is:

$$\hat{\boldsymbol{\mu}} = \hbar\gamma \sum_{k=1}^n \hat{\mathbf{I}}_k, \quad (1.174)$$

where  $\hat{\mathbf{I}}_k$  is the spin operator for a nucleus  $k$  such that:

$$\hat{\mathbf{I}}_k = (\hat{I}_{kx}\mathbf{e}_x + \hat{I}_{ky}\mathbf{e}_y + \hat{I}_{kz}\mathbf{e}_z). \quad (1.175)$$

The total nuclear magnetization of the sample is given by:

$$\mathbf{M} = \frac{\sum_{k=1}^n \hat{\boldsymbol{\mu}}}{V_s} = \frac{c_s V_s \langle \bar{\hat{\boldsymbol{\mu}}} \rangle}{V_s} = c_s \langle \bar{\hat{\boldsymbol{\mu}}} \rangle, \quad (1.176)$$

where  $\langle \bar{\hat{\boldsymbol{\mu}}} \rangle$  is the ensemble average of the expectation value of the magnetic dipole moment.

This magnetization leads to the signal obtained in NMR, to find the relationship the principle of reciprocity is invoked [82]. Consider the induction field,  $\mathbf{B}_1$ , produced by a coil carrying unit current. For a magnetic dipole,  $\mathbf{m}$ , the induced emf is given by:

$$\xi = -\frac{\partial}{\partial t} \{\mathbf{B}_1 \cdot \mathbf{m}\}, \quad (1.177)$$

where  $\mathbf{B}_1$  is the field produced by the unit current in the coil at  $\mathbf{m}$ . It follows that for a sample, after being subjected to a  $(\pi/2)$  pulse, only the value of  $\mathbf{B}_1$  at all points within the sample is needed to be able to calculate the emf induced in the coil, if  $\mathbf{M}$  lies in the  $xy$ -plane:

$$\xi = - \int_{\text{sample}} \frac{\partial}{\partial t} \{\mathbf{B}_1 \cdot \mathbf{M}\} dV_s, \quad (1.178)$$

if  $\mathbf{B}_1$  is assumed to be homogeneous over the sample volume this gives:

$$\xi = \frac{\partial}{\partial t} \{\mathbf{B}_1 \cdot \mathbf{M}\} V_s, \quad (1.179)$$

Substitution of the result from Eqn. 1.176 gives

$$\xi = \frac{\partial}{\partial t} \{\mathbf{B}_1 \cdot \langle \bar{\hat{\boldsymbol{\mu}}} \rangle c_s\} V_s, \quad (1.180)$$

if the  $B_1$  coil is aligned along the  $x$ -axis, only the  $x$ -axis components contribute to the emf

$$\xi = \frac{\partial}{\partial t} \{B_{1x} \langle \bar{\hat{\mu}}_x \rangle c_s\} V_s, \quad (1.181)$$

using Eqn. 1.174,  $\langle \hat{\mu}_x \rangle = \hbar \gamma \langle \hat{I}_x \rangle$  the emf becomes

$$\xi = \frac{\partial}{\partial t} \{B_{1x} \langle \bar{\hat{I}}_x \rangle c_s\} V_s \hbar \gamma, \quad (1.182)$$

from 1.2.4, the ensemble average can be found using the density operator  $\langle \hat{I}_x \rangle = \text{Tr}\{\hat{\rho} \hat{I}_x\}$  so

$$\xi = \frac{\partial}{\partial t} \{B_{1x} [\text{Tr}\{\hat{\rho} \hat{I}_x\}] c_s\} V_s \hbar \gamma. \quad (1.183)$$

For a spin-1/2 nucleus this equation becomes:

$$\xi = \frac{\partial}{\partial t} \{B_{1x} [\rho_- + \rho_+] c_s\} V_s \hbar \gamma \frac{1}{2}, \quad (1.184)$$

if all terms apart from the coherences are considered time independent, the emf can be simplified for now as

$$\xi \sim \frac{\partial}{\partial t} \rho_{-}(t) + \frac{\partial}{\partial t} \rho_{+}(t), \quad (1.185)$$

using Eqn. 1.163

$$\rho_{-}(t) = \rho_{-}(0) \exp\{(i\omega^0 - \lambda)t\} \quad (1.186)$$

$$\rho_{+}(t) = \rho_{+}(0) \exp\{(-i\omega^0 - \lambda)t\}, \quad (1.187)$$

the emf becomes

$$\xi \sim (i\omega^0 \rho_{-} - i\omega^0 \rho_{+}), \quad (1.188)$$

the signal that one obtains in an NMR experiment is proportional to the emf induced in the pick-up coil this is denoted  $s_{\text{FID}}$  and is given by:

$$s_{\text{FID}} \sim (i\omega^0 \rho_{-} - i\omega^0 \rho_{+}) \frac{1}{2} \frac{B_1}{i} \gamma \hbar c_s V_s. \quad (1.189)$$

#### 1.2.11.1 Quadrature detection

This 'raw' NMR signal typically oscillates at many hundred megahertz which is too fast for conversion to a digital signal that can be interpreted on a computer. Therefore, it is necessary to down convert the frequency of the NMR signals. This is accomplished by subtracting a frequency that is close to the Larmor frequency, typically, the frequency subtracted is set somewhere in the middle of the spectrum. This frequency, generated locally by an r.f. synthesiser, is called the reference frequency. It is denoted  $\omega_{\text{ref}}$  and has an associated phase  $\phi_{\text{ref}}$

This process of subtraction is carried out by multiplying together the two input signals in a mixer. The signal from the FID is multiplied by the receiver reference signal:

$$s_{\text{rec}}(t) = \cos(\omega_{\text{ref}}t + \phi_{\text{rec}}), \quad (1.190)$$

the reference signal is split into two parts  $A$  and  $B$  where  $A$  has the same form as above and  $B$  is given an additional phase shift so:

$$s_{\text{rec}}^A(t) = \cos(\omega_{\text{ref}}t + \phi_{\text{rec}}) \quad (1.191)$$

$$s_{\text{rec}}^B(t) = \cos(\omega_{\text{ref}}t + \phi_{\text{rec}} + \pi/2). \quad (1.192)$$

The signal after mixing with  $A$  is:

$$s_{\text{FID}}(t) s_{\text{rec}}^A(t) = (i\omega^0 \rho_{-}(t) - i\omega^0 \rho_{+}(t)) \cos(\omega_{\text{ref}}t + \phi_{\text{rec}}), \quad (1.193)$$

which can be evaluated as

$$s_{\text{FID}}(t)s_{\text{rec}}^A(t) = \frac{1}{2}i\rho_{-}(0)\exp\{i[(\omega^0 + \omega_{\text{ref}})t + \phi_{\text{rec}}]\}e^{-\lambda t} \quad (1.194)$$

$$+ \frac{1}{2}i\rho_{-}(0)\exp\{i[(\omega^0 - \omega_{\text{ref}})t - \phi_{\text{rec}}]\}e^{-\lambda t} \quad (1.195)$$

$$- \frac{1}{2}i\rho_{+}(0)\exp\{i[-(\omega^0 - \omega_{\text{ref}})t + \phi_{\text{rec}}]\}e^{-\lambda t} \quad (1.196)$$

$$+ \frac{1}{2}i\rho_{+}(0)\exp\{i[-(\omega^0 + \omega_{\text{ref}})t - \phi_{\text{rec}}]\}e^{-\lambda t}. \quad (1.197)$$

This rather complicated signal is now passed through a low pass r.f. filter which removes the high frequency components, this removes the components oscillating at  $\omega^0 + \omega_{\text{ref}}$  and retains the low frequency components  $\Omega^0 = \omega^0 - \omega_{\text{ref}}$ . The signal  $s_A(t)$  emerging from the filter is

$$s_A = + \frac{1}{2}i\rho_{-}(0)\exp\{i(\Omega^0 t - \phi_{\text{rec}})\}e^{-\lambda t} \quad (1.198)$$

$$- \frac{1}{2}i\rho_{+}(0)\exp\{i(-\Omega^0 t + \phi_{\text{rec}})\}e^{-\lambda t}, \quad (1.199)$$

due to the relationship between laboratory and rotating-frame coherences from Eqn. 1.141 this can be written as

$$s_A = + \frac{1}{2}i\tilde{\rho}_{-}(0)\exp\{i(\Omega^0 t - \phi_{\text{rec}} + \phi_{\text{ref}})\}e^{-\lambda t} \quad (1.200)$$

$$- \frac{1}{2}i\tilde{\rho}_{+}(0)\exp\{i(-\Omega^0 t + \phi_{\text{rec}} - \phi_{\text{ref}})\}e^{-\lambda t}, \quad (1.201)$$

where  $\phi_{\text{ref}}$  represents the angle of the rotating frame with respect to the laboratory frame at time  $t = 0$ . The equations for the precession in the rotating frame (Eqn. 1.163) allow for the simplification

$$s_A = + \frac{1}{2}i\tilde{\rho}_{-}(t)\exp\{-i(\phi_{\text{rec}} - \phi_{\text{ref}})\} - \frac{1}{2}i\tilde{\rho}_{+}(t)\exp\{i(\phi_{\text{rec}} - \phi_{\text{ref}})\}. \quad (1.202)$$

The same arguments can be repeated for the phase shifted signal path  $B$

$$s_B = + \frac{1}{2}i\tilde{\rho}_{-}(t)\exp\{-i(\phi_{\text{rec}} - \phi_{\text{ref}})\} + \frac{1}{2}i\tilde{\rho}_{+}(t)\exp\{i(\phi_{\text{rec}} - \phi_{\text{ref}})\}. \quad (1.203)$$

These signals are treated as two components of one complex signal:

$$s(t) = s_A(t) + is_B(t), \quad (1.204)$$

which evaluates to

$$s(t) \sim i\tilde{\rho}_{-}(t)\exp\{-i(\phi_{\text{rec}} - \phi_{\text{ref}})\}. \quad (1.205)$$

Which contains contributions from the rotating frame  $(-1)$ -quantum coherences. The  $(+1)$ -quantum coherences have disappeared however, the contribution is equal to the  $(-1)$ -quantum coherence so a factor two is included the frame phase shift as well as

other sources of constant shifts from instrumentation are corrected in post-processing so the quadrature signal can be expressed as:

$$s(t) \sim 2i\tilde{\rho}_-(t)\exp\{-i\phi_{\text{rec}}\}. \quad (1.206)$$

There are some time independent variables from the original expression of  $s_{\text{FID}}$  which can now be included, and neglecting the the noise and gain acquired from quadrature demodulation, these signals are:

$$s(t) = 2i\omega^0 \frac{1}{2} \frac{B_{1x}}{i_c} \gamma \hbar c_s V_s \tilde{\rho}_-(t) \exp\{-i\phi_{\text{rec}}\} \quad (1.207)$$

$$s(t) = i\omega^0 \frac{B_{1x}}{i_c} \gamma \hbar c_s V_s \tilde{\rho}_-(t) \exp\{-i\phi_{\text{rec}}\}, \quad (1.208)$$

where  $\omega^0$  is the Larmor frequency,  $B_{1x}/i_c$  is the coil sensitivity,  $\gamma$  is the gyromagnetic ratio,  $\hbar$  is the reduced Planck's constant, the term  $c_s V_s$  is the number of spins in the sample.

#### 1.2.11.2 Signal after a pulse

The signal dependence can be seen more clearly if one gets more quantitative, to do this, consider a  $(\pi/2)_x$  pulse with receiver phase,  $\phi_{\text{rec}} = 0$ , for brevity the tilde will be dropped as only the rotating frame will be considered. In order to calculate the  $(-1)$ -quantum coherence, the density operator must be calculated first. Using definitions from Eqn. 1.131 and Eqn. 1.133, the rotating frame density operator at equilibrium is

$$\hat{\rho}^{eq} = \frac{1}{2}\mathbb{1} + \frac{1}{2}\mathbb{B}\hat{I}_z, \quad (1.209)$$

immediately after the pulse at  $t = 0$  the density operator is

$$\hat{\rho}(0) = \frac{1}{2}\mathbb{1} - \frac{1}{2}\mathbb{B}\hat{I}_y, \quad (1.210)$$

this can be written in terms of the shift and projection operators:

$$\hat{\rho}(0) = \frac{1}{2}\hat{I}^\alpha + \frac{1}{2}\hat{I}^\beta - \frac{1}{4i}\mathbb{B}\hat{I}^+ + \frac{1}{4i}\mathbb{B}\hat{I}^-, \quad (1.211)$$

the  $(-1)$ -quantum coherence is equal to the coefficient of the  $\hat{I}^-$  operator

$$\rho_-(0) = \frac{1}{4i}\mathbb{B}, \quad (1.212)$$

the coherence at a time  $t > 0$  is given by:

$$\rho_-(t) = \rho_-(0)\exp\{i\Omega^0 - \lambda)t\}. \quad (1.213)$$

By combining this with the signal equation:

$$s(t) = a \exp\{(i\Omega^0 - \lambda)t\}, \quad (1.214)$$

where the signal amplitude  $a$  is

$$a = i\omega^0 \frac{B_{1x}}{i_c} \gamma \hbar c_s V_s \rho_-(0) \exp\{-i\phi_{\text{rec}}\}, \quad (1.215)$$

and in the case of the  $(\pi/2)_x$  pulse

$$a = i\omega^0 \frac{B_{1x}}{i_c} \gamma \hbar c_s V_s \frac{1}{4i} \mathbb{B}, \quad (1.216)$$

collecting like terms and expanding  $\mathbb{B}$  gives

$$a = \frac{1}{4} \frac{B_{1x}}{i_c} \gamma^3 \hbar^2 B_0^2 \frac{n_s}{k_b T}, \quad (1.217)$$

where  $n_s$  is the number of spins in the sample. This relationship makes sense intuitively as increasing the number of spins in the sample leads to an increase in signal amplitude as does increasing the coil sensitivity.

### 1.2.11.3 Chemical Shift and J-coupling

In a molecule, nuclei are surrounded by clouds of electrons which can shield, or de-shield, it from the effects of the external field  $B_0$ .

The chemical shielding factor,  $\sigma$ , shifts the resonance frequency of the nuclear spin. It can now include it in Eqn. 1.73:

$$\omega_j^0 = -\gamma_j B_0 (1 - \sigma), \quad (1.218)$$

this chemical shielding is specific to each nuclei position in the molecule. It is possible for two or more nuclei to share the same factor. These are referred to as being 'chemically equivalent'.

The shielding is often around  $10^{-6}$  for  $^1\text{H}$ , when plotting and examining spectra it would not be useful to use absolute frequencies, as discussed they are regularly in the hundreds of MHz, whereas the differences in peaks might only be kHz or less. To combat this a relative frequency scale is used called chemical shift,  $\delta$ , defined as:

$$\delta = \frac{\omega_j - \omega_j^{\text{ref}}}{\omega_j^{\text{ref}}}, \quad (1.219)$$

where  $\omega_j$  is the precession frequency of the nucleus of interest, and  $\omega_j^{\text{ref}}$  is the precession frequency of a reference nucleus.  $\delta$  is a dimensionless number, unaffected by magnetic

field strength, it is often small compared to the size of the field and is reported in parts per million (ppm).

In addition to the external  $B_0$  field, the nuclear spins are also affected by the magnetic fields generated by neighbouring spins. These magnetic fields are mediated by the electrons in the chemical bonds. This is referred to as spin-spin coupling or  $J$ -coupling and gives rise to peak splittings in spectra. These splittings, and therefore the values of  $J$ -couplings, range from a few Hz to a thousand Hz typically. These become important when considering the Hamiltonian of a multi-spin system but are not discussed in this work.

Both of these,  $\sigma$  and  $J$ -couplings, are tensors this means they depend on the orientation of the molecule and the spin with respect to the magnetic field. In liquids, however, tumble rapidly compared to the timescale of an NMR experiment. This averages the interactions resulting in a scalar quantity for each.

There are additional effects the nuclear spins experience, for example, dipole-dipole coupling which is a through space spin-spin coupling, and quadrupole coupling where there are spins with  $>1/2$  values however, these are not relevant to this work.



## 1.3 Micro-NMR

All NMR experiments depend on two performance metrics: sensitivity and resolution. Sensitivity refers to the minimum number of spins needed to give a signal clearly above the noise, whilst resolution quantifies how well different species in the sample can be differentiated. These two properties are often linked, by selecting a smaller sample it is possible to enhance resolution by detecting a smaller portion of spins in the sample but this compromises sensitivity as the number of spins become more limited.

In NMR, nuclear spin state coherences have long lifetimes that are governed by the decay constant,  $T_2$ , which is typically seconds, but in some cases can be minutes long. These long lifetimes contribute to extremely narrow lines in the spectrum, with resolutions of one part per billion regularly achieved in commercial systems.

### 1.3.1 Sensitivity

#### 1.3.1.1 Signal to noise ratio

Sensitivity in NMR at thermal equilibrium is always in short supply. In an NMR experiment, the signal amplitude after a  $\pi/2$  pulse at thermal equilibrium,  $a$ , can be expressed as Eqn. 1.217:

$$a = \frac{1}{4} \frac{B_{1x}}{i_c} \gamma^3 \hbar^2 B_0^2 \frac{n_s}{k_B T}, \quad (1.220)$$

where,  $B_{1x}/i_c$  is the coil sensitivity,  $\gamma$  is the gyromagnetic ratio of the nucleus,  $\hbar = h/2\pi$ ,  $B_0$  is the magnetic field,  $n_s$  is the number of spins in the sample,  $k_B$  is the Boltzmann constant and  $T$  is the absolute temperature. The amplitude of the signal depends on the Boltzmann distribution of population which at room temperature is on the order of  $10^{-25}$  J which is much lower than the thermal energy of the system. From the equation, increasing  $B_0$  would seem a valid strategy and comparatively it can be, increasing from 14.1T to 23.5T can almost triple the signal amplitude, however even at 23.5T there is only a factor of  $6 \times 10^{-6}$  in population difference. It's this very small value that is responsible for the low sensitivity of NMR compared to other techniques.

As mentioned, detection in NMR is typically done through the induction of a voltage in a coil that's close to the precessing nuclear spins, this is usually referred to as the sample coil. Unfortunately, this coil also brings with it a type of interference, noise, analogous to the 'hiss' in the background of radio it is produced mainly from thermal motion of electrons in the sample coil with some contribution from thermal motion of ions in solution. The signal to noise ratio, SNR, is an important factor in NMR experiments if it's too low the signal will never be seen.

The SNR was formulated by Abragam[83] and the analysis extended by Hoult and Richards[82] and is defined as the peak signal divided by the root mean square

(rms) noise. By including the amplitude from Eqn. 1.217 and using the *Rayleigh-Jeans approximation* for the noise the SNR is:

$$\text{SNR} = \frac{k_0 \frac{1}{4} \frac{B_1}{i_c} \gamma^3 \hbar^2 B_0^2 \frac{n_s}{k_b T_s}}{F \sqrt{4 k_b T_c R_{\text{noise}} \Delta f}}, \quad (1.221)$$

where  $k_0$  is a factor that accounts for inhomogeneity in the  $B_1$  field,  $T_s$  is the temperature of the sample, and  $n_s$  is the number of spins in the sample. The factor  $B_1/i_c$  the magnetic field from the coil per unit current is defined as the coil sensitivity. The denominator is the noise determined by the noise factor from the spectrometer ( $F$ ) and the dissipative losses,  $R_{\text{noise}}$ , of the coil, circuit and sample for the spectral bandwidth  $\Delta f$ .  $T_c$  is the absolute temperature of the coil, and  $k_b$  is the Boltzmann constant.

In the same paper, Hoult and Richards introduced the principle of reciprocity for calculating the sensitivity of the RF coil. This states that the signal received from a sample by a coil is proportional to the magnetic field which would have been created in the sample if unit current were passed through the coil. Therefore the SNR is directly proportional to the sensitivity of the coil,  $B_1/i_c$ . This can be seen if an effective sample volume is defined, that is the volume in which  $B_1$  is within 10% of the maximum value at the centre of the coil. The SNR is given by a more simple expression[84]:

$$\text{SNR} = C \frac{B_1 n_s}{i_c \sqrt{R \Delta f}}, \quad (1.222)$$

where  $n_s$  is the number of spins in located within an effective volume. For protons at 600MHz the constant,  $C$  equals  $1.4 \times 10^{-11}$  in SI units ( $B_0 = 14.1\text{T}$ ,  $T = 300\text{K}$ ,  $\gamma = 0.2675 \times 10^9 \text{ radT}^{-1}\text{s}^{-1}$ ,  $I = 1/2$  and  $F = 1$  assuming negligible noise from the spectrometer.)

From the simple expression it becomes clear that the way to improve SNR is to increase the filling factor, maximise coil sensitivity,  $B_1/i_c$ , and minimise the total resistance. The filling factor,  $\alpha_F$  is given by:

$$\alpha_F = \frac{\int B_1^2 \rho(r) dV}{\int B_1^2 dV}, \quad (1.223)$$

where the function  $\rho$  is unity in the sample area, and zero elsewhere. For a long solenoid coil with the interior space filled with sample,  $\alpha_F = 1/2$ .

Increasing the filling factor and maximising coil sensitivity, can be solved by decreasing the size of the detector. The third, minimising resistance in the coil, can be tackled by commercially available cryo-probes where the coil is cooled with a stream of He gas to 20K this reduces the thermal noise from the source and can increase SNR by a factor of four.

To see how size of coil affects SNR, consider an RF helical coil. An idealised coil is a cylindrical shell with uniform current density. The RF current penetrates to a frequency specific depth  $\delta_{\text{RF}}$ . For copper at 600 MHz and room temperature  $\delta_{\text{RF}} = 2.7 \mu\text{m}$ . The centre field is given by:

$$\frac{B_1}{i_c} = \frac{\mu_0}{\sqrt{l^2 + d^2}}. \quad (1.224)$$

Resistance is:

$$R = \rho_r \frac{\pi d}{l\delta}, \quad (1.225)$$

with  $l$ , the height of the copper cylinder,  $d$  the diameter and  $\rho_r$  the resistivity. Optimum coil sensitivity is given by  $d/l = 1$  in this case the signal to noise is:

$$SNR = 0.9 \times 10^{-16} \frac{n_s}{d\sqrt{\Delta f}}, \quad (1.226)$$

for a fixed number of spins the SNR scales with  $1/d$  as predicted by [82]

### 1.3.2 Signal Averaging

In NMR, the total signal that emerges from the probe contains signal from the sample under observation as well as uncontrolled random signals called noise. In NMR spectroscopy, the most dominant source of noise comes from the thermal motions of the electrons in the receiver coil, called thermal noise. In order for the signal that originated from the sample to rise above the noise, signal averaging must be employed. This works as the sum of two identical experiments is twice the signal of the original individual experiment:

$$s_{\text{NMR}}(1+2) = s_{\text{NMR}}(1) + s_{\text{NMR}}(2) = 2s_{\text{NMR}}(1). \quad (1.227)$$

The key, is that this relationship does not apply equally to the noise, as it is random. A suitable definition of the noise amplitude in a single experiment is given by the root mean square (RMS) noise defined as:

$$\sigma_{\text{noise}} = \langle s_{\text{noise}}(1)^2 \rangle^{1/2}, \quad (1.228)$$

where the angle bracket indicates an average over all sampling points.

As in 1.2.11, the signal generated by the noise is proportional to the noise voltage in the coil such that:

$$\langle s_{\text{noise}}(1)^2 \rangle \sim (\langle \xi_n^2 \rangle), \quad (1.229)$$

where  $\langle \xi_n^2 \rangle$  is the mean square emf produced in the coil by thermal noise, and  $F$  is the noise factor from the spectrometer.

This mean square emf is derived from statistical mechanics and can be expressed as [85, 86]:

$$\langle \xi_n^2 \rangle = 4k_b T_C R_{\text{noise}} \Delta f. \quad (1.230)$$

Including a factor for the noise from the spectrometer,  $F$ ,  $\sigma_{\text{noise}}$  can be expressed quantitatively as:

$$\sigma_{\text{noise}} = F \sqrt{4k_b T_C R_{\text{noise}} \Delta f}, \quad (1.231)$$

which is equal to the denominator for the SNR from Eqn. 1.221.

The RMS noise is the same for two experiments assuming the noise is stationary i.e. the noise does not change from one experiment to the next. However, this does not imply that the noise from two experiments has twice the value. Summed over the two experiments the RMS noise takes the value:

$$\sigma_{\text{noise}}(1+2) \cong \sqrt{2} \sigma_{\text{noise}}(1). \quad (1.232)$$

Since the noise over two experiments increases by  $\sqrt{2}$  but the signal doubles. Therefore the signal to noise ratio over two experiments can be written as:

$$\text{SNR}(1+2) = \sqrt{2} \frac{s_{\text{NMR}}(1)}{\sigma_{\text{noise}}(1)}. \quad (1.233)$$

This can be extended to show the signal-to-noise over  $N$  transients is a factor  $\sqrt{N}$  larger than the signal for a single transient. So by signal averaging over many scans the SNR can be increased.

In principle, this allows NMR signals that have a SNR less than one to be 'pulled out' of the noise. In reality, this is time consuming as in order to repeat an experiment precisely it is essential to allow the spin system to reach thermal equilibrium again. The different NMR experiments must therefore be separated by an interval many times longer than  $T_1$ , which in some case can be several seconds. For example, if the SNR of the first experiment is 0.1 clearly the signal will be buried in the noise. The SNR may be changed to 10:1 by signal averaging over 10,000 scans. If each scan takes 1 second this amounts to 3 hours of instrument time which is long but acceptable. However, if the SNR is 0.01 then it follows that 300 hours would now be needed which is not feasible.

In order for smaller signals to be detected, the amount of signal i.e. the amount of polarization in the sample, needs to be increased this can be done by preparing the sample in a specific way and is referred to as 'hyperpolarization'.

### 1.3.3 Limit of Detection

The signal to noise ratio can be found in the time or frequency domain. In the time domain the root mean square noise,  $\sigma_{\text{noise}}$ , is proportional to  $\sqrt{\Delta f}$ . Therefore the SNR in the time domain is not a good measure of sensitivity, it can be artificially inflated by narrowing the bandwidth. Instead it is better to use *limit of detection*, defined as the number of spins that have to resonate within a bandwidth of 1 Hz to give an SNR of 3. This gives the normalised limit of detection as[87]:

$$\text{nLOD}_t = \frac{3n_s}{\text{SNR}_t \sqrt{\Delta f}}. \quad (1.234)$$

Where  $n_s$  is the number of spins that were present in the sample for the measurement and  $\text{SNR}_t$  is the signal to noise ratio in the time domain. In the frequency domain, this becomes

$$\text{nLOD}_\omega = \frac{3n_s \sqrt{\Delta t}}{\text{SNR}_\omega}, \quad (1.235)$$

here,  $\Delta t$  is the effective acquisition time for a single scan, given by the inverse of the line broadening applied in the processing of the spectrum.

Practically, NMR relies on signal averaging (see 1.3.2) to enhance the spectra. This method requires waiting between scans for the spins to reach thermal equilibrium. In this case, a better measure of sensitivity can be applied by using total measurement time as  $\Delta t$ . In this case the limit of detection now depends on instrumentation and sample as  $T_1$  relaxation dictates the experiment repetition rate.

### 1.3.4 Concentration limit of detection

Both types of LOD discussed so far are absolute measures. It is often of more interest to examine the *concentration* limit of detection cLOD. This is given by dividing the LOD by the sample volume:

$$\text{cLOD} = \frac{\text{nLOD}}{V_s} = \frac{\text{nLOD}}{\alpha_f V_c}. \quad (1.236)$$

Where  $V_c$  is the volume of the coil and  $\alpha_f$  is the filling factor defined in Eqn. 1.223.

Eqn. 1.235 shows that overall, the mass sensitivity of a probe is inversely proportional to SNR. It follows from Eqn. 1.226, that the reduction in coil size would lead to a reduction of nLOD. This relationship has been a key driving force in the development of micro-NMR, however, a coil size reduction of a factor of 2, reduces the volume by a factor of 8 leading to a rise in cLOD. For a *concentration* limited sample, it is more important to have as high a volume as possible to increase the number of spins available for detection. For a *mass* limited sample, the number of spins is fixed so it is more advantageous to reduce the size of the coil.

### 1.3.5 Transmission line probe

This work employs a planar transmission line probe (TLP) [88, 89], in which the geometry differs from that of a classic micro-coil. The design of the TLP is based off early work by van Bentum *et al.* and for an equivalent helix gives  $\sqrt{2}$  larger SNR [84]. The TLP geometry, shown in Fig. 1.7, features two conducting planes of a specific length with a constriction in the centre. This geometry, gives rise to an electromagnetic eigenmode with a strong anti-node of the magnetic field between the two planes at the constriction. This concentrates the r.f. field and the detection sensitivity onto the sample area. The probe is compatible with a generic microfluidic device that has well defined outer geometry, and a fixed sample chamber position. The main advantage of using this probe is

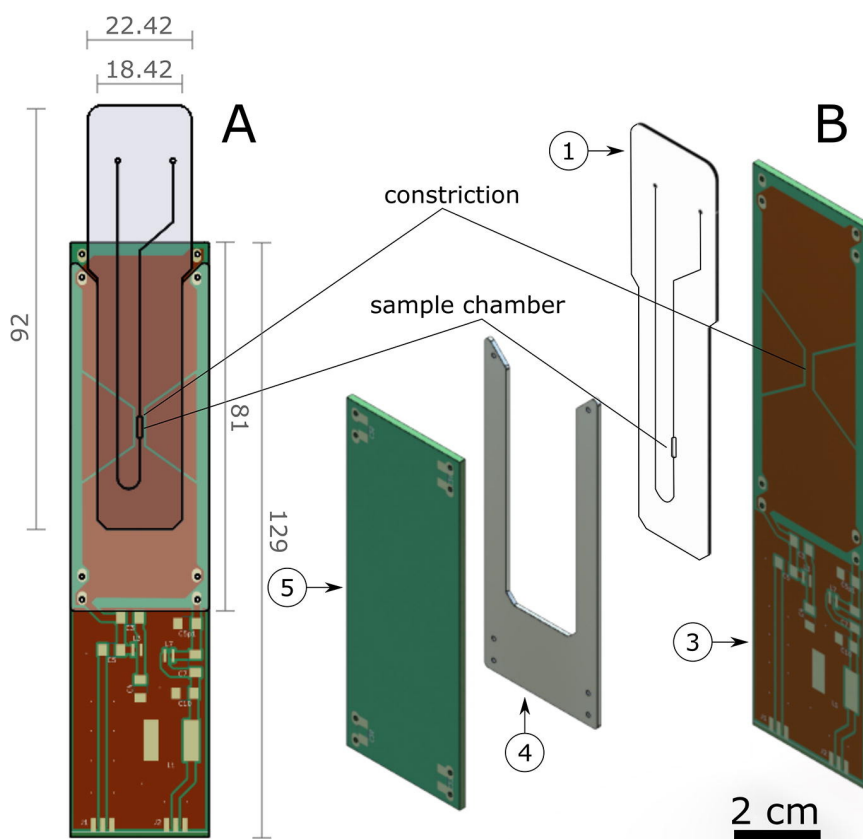


FIGURE 1.7: Drawings of the detector assembly and the microfluidic device (1). A: front view (dimensions in mm); B: exploded view. Spacer (4) ensures the alignment of the sample chamber with the constrictions on the PCB planes. In A, PCB plane 5 is hidden to show the orientation of 1 with respect to PCB plane 3. Thickness of each of the PCB planes is 1.52 mm and the copper layers on the PCBs is 35  $\mu$  m. Both the microfluidic device and the spacer are made from PMMA and have thickness of 0.9 mm and 1 mm respectively. Figure reproduced from [89].

the compatibility of the device with customisable microfluidic devices, allowing a broad range of applications such as tissue culture, microfluidic droplets, cell culture, and hydrogenation on a chip [89]. These applications can be couple with pratical NMR using the TLP, which few other microprobes allow [90–92]. The limit of detection LOD for

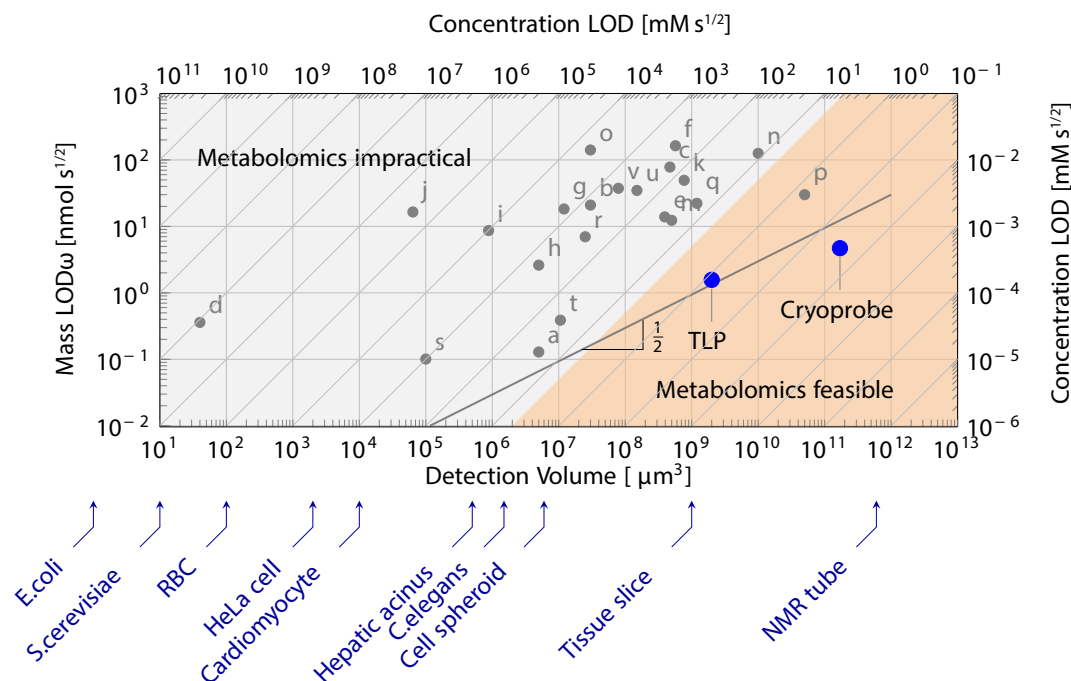


FIGURE 1.8: Plot comparing the limits of detection of previously design micro-NMR detectors. Letters a-t correspond to different authors as cited by Badilata *et al.* [87] Letters u [93] and t [90] represent more recent work. The probe used here is labelled at TLP and a commercial cryo-probe is shown for reference.

the TLP used is  $1.4 \text{ nmol s}^{1/2}$  which comparatively lower than detectors of a similar size and more similar to the LOD of commercial cryo-probes mentioned previously. Where the probe is exceptional in terms of micro-detector is the cLOD, this is demonstrated in Fig. 1.8 which shows a wide variety of micro-NMR detectors that have been reported in the literature. Fig. 1.8 has detection volume and mass LOD (nLOD) plotted logarithmically on the  $x$ -axis and  $y$ -axis respectively, the diagonal lines represent constant concentration (cLOD). The general trend of decreasing nLOD with size is indicated with a line of gradient  $1/2$ . The area shaded orange that is defined as the 'metabolomics feasible' range is a maximum  $5 \text{ mM } \sqrt{s}$  ensuring species present at  $0.1 \text{ mM}$  can be detected within less than 20 mins. The TLP has a cLOD of  $1 \text{ mM } \sqrt{s}$  and can detect species at  $0.02 \text{ mM}$  in that time frame. Whilst this is suitable for some metabolomic information to be gained, however, the subtle changes in molecules present at less than  $0.02 \text{ mM}$  are of interest but are unreachable with this probe using thermal polarisation at this time.

For this work, the goal is not only to combine NMR detection and microfluidics, clearly that has been done before. However, it is the combination of these two in a way that does not minimise compromises on either side: free fluidic design and complexity on the one hand, and the full resolution and sensitivity of conventional liquid state NMR spectroscopy on the other.

# Bibliography

- [1] S. Terry, J. Jerman and J. Angell, *IEEE Transactions Electron Devices*, 1979, **26**, 1880.
- [2] D. R. Reyes, D. Iossifidis, P.-A. Auroux and A. Manz, *Analytical Chemistry*, 2002, **74**, 2623–2636.
- [3] H. Van Lintel, F. Van de Pol and S. Bouwstra, *Sensors and Actuators*, 1988, **15**, 153–167.
- [4] F. Van De Pol, D. Wonnink, M. Elwenspoek and J. Fluitman, *Sensors and Actuators*, 1989, **17**, 139–143.
- [5] S. Shoji, M. Esashi and T. Matsuo, *Sensors and Actuators*, 1988, **14**, 101–107.
- [6] A. Manz, Y. Miyahara, J. Miura, Y. Watanabe, H. Miyagi and K. Sato, *Sensors and Actuators B: Chemical*, 1990, **1**, 249–255.
- [7] A. Manz, N. Graber and H. á. Widmer, *Sensors and Actuators B: Chemical*, 1990, **1**, 244–248.
- [8] A. Manz, D. Harrison, J. Fettingner, E. Verpoorte, H. Ludi and H. Widmer, TRANSDUCERS’91: 1991 International Conference on Solid-State Sensors and Actuators. Digest of Technical Papers, 1991, pp. 939–941.
- [9] D. J. Harrison, A. Manz, Z. Fan, H. Luedi and H. M. Widmer, *Analytical Chemistry*, 1992, **64**, 1926–1932.
- [10] K. Seiler, D. J. Harrison and A. Manz, *Analytical Chemistry*, 1993, **65**, 1481–1488.
- [11] A. T. Woolley, D. Hadley, P. Landre, A. J. deMello, R. A. Mathies and M. A. Northrup, *Analytical Chemistry*, 1996, **68**, 4081–4086.
- [12] L. Bousse, R. McReynolds, G. Kirk, T. Dawes, P. Lam, W. Bemiss and J. Parce, *Sensors and Actuators B: Chemical*, 1994, **20**, 145–150.
- [13] G. M. Whitesides, *Nature*, 2006, **442**, 368–73.
- [14] J. M. Ng, I. Gitlin, A. D. Stroock and G. M. Whitesides, *Electrophoresis*, 2002, **23**, 3461–3473.



- [15] G. M. Whitesides and A. D. Stroock, *Physics Today*, 2001, **54**, 42–48.
- [16] J. C. McDonald, D. C. Duffy, J. R. Anderson, D. T. Chiu, H. Wu, O. J. Schueller and G. M. Whitesides, *ELECTROPHORESIS: An International Journal*, 2000, **21**, 27–40.
- [17] D. B. Weibel, M. Kruithof, S. Potenta, S. K. Sia, A. Lee and G. M. Whitesides, *Analytical Chemistry*, 2005, **77**, 4726–4733.
- [18] A. Günther, M. Jhunjhunwala, M. Thalmann, M. A. Schmidt and K. F. Jensen, *Langmuir*, 2005, **21**, 1547–1555.
- [19] D. J. Laser and J. G. Santiago, *Journal of micromechanics and microengineering*, 2004, **14**, R35.
- [20] C. L. Hansen, E. Skordalakes, J. M. Berger and S. R. Quake, *Proceedings of the National Academy of Sciences*, 2002, **99**, 16531–16536.
- [21] R. Ramsey and J. Ramsey, *Analytical Chemistry*, 1997, **69**, 1174–1178.
- [22] A. R. Wheeler, W. R. Throdsset, R. J. Whelan, A. M. Leach, R. N. Zare, Y. H. Liao, K. Farrell, I. D. Manger and A. Daridon, *Analytical Chemistry*, 2003, **75**, 3581–3586.
- [23] C.-C. Lee, G. Sui, A. Elizarov, C. J. Shu, Y.-S. Shin, A. N. Dooley, J. Huang, A. Daridon, P. Wyatt, D. Stout *et al.*, *Science*, 2005, **310**, 1793–1796.
- [24] T. Thorsen, R. W. Roberts, F. H. Arnold and S. R. Quake, *Physical review letters*, 2001, **86**, 4163.
- [25] D. Link, S. L. Anna, D. Weitz and H. Stone, *Physical review letters*, 2004, **92**, 054503.
- [26] Y.-C. Tan, J. S. Fisher, A. I. Lee, V. Cristini and A. P. Lee, *Lab on a Chip*, 2004, **4**, 292–298.
- [27] Z. Nie, S. Xu, M. Seo, P. C. Lewis and E. Kumacheva, *Journal of the American Chemical Society*, 2005, **127**, 8058–8063.
- [28] T. Nisisako and T. Torii, *Advanced materials*, 2007, **19**, 1489–1493.
- [29] A. Utada, E. Lorenceau, D. Link, P. Kaplan, H. Stone and D. Weitz, *Science*, 2005, **308**, 537–541.
- [30] A. Huebner, M. Srisa-Art, D. Holt, C. Abell, F. Hollfelder, J. Edel *et al.*, *Chemical communications*, 2007, 1218–1220.
- [31] T. Thorsen, R. W. Roberts, F. H. Arnold and S. R. Quake, *Physical review letters*, 2001, **86**, 4163.

- [32] F. K. Balagaddé, L. You, C. L. Hansen, F. H. Arnold and S. R. Quake, *Science*, 2005, **309**, 137–140.
- [33] P. J. Hung, P. J. Lee, P. Sabounchi, R. Lin and L. P. Lee, *Biotechnology and bioengineering*, 2005, **89**, 1–8.
- [34] S. Takayama, E. Ostuni, P. LeDuc, K. Naruse, D. E. Ingber and G. M. Whitesides, *Nature*, 2001, **411**, 1016.
- [35] J. Voldman, M. Gray, M. Toner and M. Schmidt, *Analytical Chemistry*, 2002, **74**, 3984–3990.
- [36] Z. Wang, J. El-Ali, M. Englund, T. Gotsaed, I. Perch-Nielsen, K. B. Mogensen, D. Snakenborg, J. P. Kutter and A. Wolff, *Lab on a Chip*, 2004, **4**, 372–377.
- [37] D. Di Carlo, K.-H. Jeong and L. P. Lee, *Lab on a Chip*, 2003, **3**, 287–291.
- [38] S.-W. Lee and Y.-C. Tai, *Sensors and Actuators A: Physical*, 1999, **73**, 74–79.
- [39] H. Lu, S. Gaudet, M. A. Schmidt and K. F. Jensen, *Analytical Chemistry*, 2004, **76**, 5705–5712.
- [40] Y. Li, J. S. Buch, F. Rosenberger, D. L. DeVoe and C. S. Lee, *Analytical Chemistry*, 2004, **76**, 742–748.
- [41] K. Sato, M. Yamanaka, H. Takahashi, M. Tokeshi, H. Kimura and T. Kitamori, *Electrophoresis*, 2002, **23**, 734–739.
- [42] T. P. Burg and S. R. Manalis, *Applied Physics Letters*, 2003, **83**, 2698–2700.
- [43] J. El-Ali, P. K. Sorger and K. F. Jensen, *Nature*, 2006, **442**, 403.
- [44] A. Folch, A. Ayon, O. Hurtado, M. Schmidt and M. Toner, *Journal of biomechanical engineering*, 1999, **121**, 28–34.
- [45] A. Folch and M. Toner, *Annual review of biomedical engineering*, 2000, **2**, 227–256.
- [46] V. L. Tsang and S. N. Bhatia, *Advanced drug delivery reviews*, 2004, **56**, 1635–1647.
- [47] A. Sivaraman, J. Leach, S. Townsend, T. Iida, B. Hogan, D. B. Stolz, R. Fry, L. Samson, S. Tannenbaum and L. Griffith, *Current drug metabolism*, 2005, **6**, 569–591.
- [48] M. J. Powers, K. Domansky, M. R. Kaazempur-Mofrad, A. Kalezi, A. Capitano, A. Upadhyaya, P. Kurzwski, K. E. Wack, D. B. Stolz, R. Kamm *et al.*, *Biotechnology and bioengineering*, 2002, **78**, 257–269.
- [49] C. Guguen-Guillouzo, B. Clément, G. Baffet, C. Beaumont, E. Morel-Chany, D. Glaize and A. Guillouzo, *Experimental cell research*, 1983, **143**, 47–54.

- [50] C. S. Chen, M. Mrksich, S. Huang, G. M. Whitesides and D. E. Ingber, *Science*, 1997, **276**, 1425–1428.
- [51] S. Bhatia, U. Balis, M. Yarmush and M. Toner, *The FASEB journal*, 1999, **13**, 1883–1900.
- [52] Y. Nakao, H. Kimura, Y. Sakai and T. Fujii, *Biomicrofluidics*, 2011, **5**, 022212.
- [53] D. Huh, B. D. Matthews, A. Mammoto, M. Montoya-Zavala, H. Y. Hsin and D. E. Ingber, *Science*, 2010, **328**, 1662–1668.
- [54] M. Esch, T. King and M. Shuler, *Annual review of biomedical engineering*, 2011, **13**, 55–72.
- [55] A. Skardal, T. Shupe and A. Atala, *Drug discovery today*, 2016, **21**, 1399–1411.
- [56] K.-J. Jang and K.-Y. Suh, *Lab on a Chip*, 2010, **10**, 36–42.
- [57] J. H. Sung and M. L. Shuler, *Lab on a Chip*, 2009, **9**, 1385–1394.
- [58] D. Huh, Y.-s. Torisawa, G. A. Hamilton, H. J. Kim and D. E. Ingber, *Lab on a Chip*, 2012, **12**, 2156–2164.
- [59] J. Wang, *Biosensors and Bioelectronics*, 2006, **21**, 1887–1892.
- [60] R. Raiteri, M. Grattarola, H.-J. Butt and P. Skládal, *Sensors and Actuators B: Chemical*, 2001, **79**, 115–126.
- [61] B. Kuswandi, J. Huskens, W. Verboom *et al.*, *Analytica chimica acta*, 2007, **601**, 141–155.
- [62] N. Pires, T. Dong, U. Hanke and N. Hoivik, *Sensors*, 2014, **14**, 15458–15479.
- [63] R. J. Flanagan, D. Perrett and R. Whelpton, *Electrochemical detection in HPLC: Analysis of drugs and poisons*, Royal Society of Chemistry, 2005, vol. 10.
- [64] P. S. Waggoner and H. G. Craighead, *Lab on a Chip*, 2007, **7**, 1238–1255.
- [65] M. Ferrari, *Nature reviews cancer*, 2005, **5**, 161.
- [66] H. Hou, X. Bai, C. Xing, N. Gu, B. Zhang and J. Tang, *Analytical Chemistry*, 2013, **85**, 2010–2014.
- [67] J. F. Rusling, C. V. Kumar, J. S. Gutkind and V. Patel, *Analyst*, 2010, **135**, 2496–2511.
- [68] A. M. Foudeh, T. F. Didar, T. Veres and M. Tabrizian, *Lab on a Chip*, 2012, **12**, 3249–3266.
- [69] S. Wang, X. Zhao, I. Khimji, R. Akbas, W. Qiu, D. Edwards, D. W. Cramer, B. Ye and U. Demirci, *Lab on a Chip*, 2011, **11**, 3411–3418.

- [70] J. R. Wojciechowski, L. C. Shriver-Lake, M. Y. Yamaguchi, E. Füreder, R. Pieler, M. Schamesberger, C. Winder, H. J. Prall, M. Sonnleitner and F. S. Ligler, *Analytical Chemistry*, 2009, **81**, 3455–3461.
- [71] N. Yildirim, F. Long, C. Gao, M. He, H.-C. Shi and A. Z. Gu, *Environmental science & technology*, 2012, **46**, 3288–3294.
- [72] A. M. Foudeh, J. T. Daoud, S. P. Faucher, T. Veres and M. Tabrizian, *Biosensors and Bioelectronics*, 2014, **52**, 129–135.
- [73] M. Swanson and B. Hammer, *Annual Reviews in Microbiology*, 2000, **54**, 567–613.
- [74] I. S. Kinstlinger and J. S. Miller, *Lab on a Chip*, 2016, **16**, 2025–2043.
- [75] P. C. Gach, K. Iwai, P. W. Kim, N. J. Hillson and A. K. Singh, *Lab on a Chip*, 2017, **17**, 3388–3400.
- [76] B. Bao, J. Riordon, F. Mostowfi and D. Sinton, *Lab on a Chip*, 2017, **17**, 2740–2759.
- [77] S. Giulitti, M. Pellegrini, I. Zorzan, P. Martini, O. Gagliano, M. Mutarelli, M. J. Ziller, D. Cacchiarelli, C. Romualdi, N. Elvassore *et al.*, *Nature cell biology*, 2019, **21**, 275–286.
- [78] J. Reboud, G. Xu, A. Garrett, M. Adriko, Z. Yang, E. M. Tukahebwa, C. Rowell and J. M. Cooper, *Proceedings of the National Academy of Sciences*, 2019, **116**, 4834–4842.
- [79] P. A. M. Dirac, *Mathematical Proceedings of the Cambridge Philosophical Society*, 1939, **35**, 416–418.
- [80] J. von Neumann, *Mathematical Foundations of Quantum Mechanics*, Princeton University Press, new edn, 2018.
- [81] F. Bloch, *Physical Review*, 1946, **70**, 460–474.
- [82] D. I. Hoult and R. E. Richards, *Journal of Magnetic Resonance (1969)*, 1976, **24**, 71–85.
- [83] A. Abragam, *The Principles of Nuclear Magnetism*, Oxford University Press, 1961.
- [84] P. J. M. van Bentum, J. W. G. Janssen, A. P. M. Kentgens, J. Bart and J. G. E. Gardeniers, *Journal of Magnetic Resonance*, 2007, **189**, 104–113.
- [85] H. Nyquist, *Physical review*, 1928, **32**, 110.
- [86] J. B. Johnson, *Physical review*, 1928, **32**, 97.
- [87] V. Badilita, R. C. Meier, N. Spengler, U. Wallrabe, M. Utz and J. G. Korvink, *Soft Matter*, 2012, **8**, 10583–10597.

- [88] G. Finch, A. Yilmaz and M. Utz, *Journal of Magnetic Resonance*, 2016, **262**, 73–80.
- [89] M. Sharma and M. Utz, *Journal of Magnetic Resonance*, 2019, **303**, 75–81.
- [90] N. Spengler, A. Moazenzadeh, R. C. Meier, V. Badilita, J. Korvink and U. Wallrabe, *Journal of Micromechanics and Microengineering*, 2014, **24**, 034004.
- [91] N. Spengler, J. Höfflin, A. Moazenzadeh, D. Mager, N. MacKinnon, V. Badilita, U. Wallrabe and J. G. Korvink, *PloS one*, 2016, **11**, e0146384.
- [92] I. Swyer, S. von der Ecken, B. Wu, A. Jenne, R. Soong, F. Vincent, D. Schmidig, T. Frei, F. Busse and H. J. Stronks, *Lab on a Chip*, 2019, **19**, 641–653.
- [93] R. C. Meier, J. Höfflin, V. Badilita, U. Wallrabe and J. G. Korvink, *Journal of Micromechanics and Microengineering*, 2014, **24**, 045021.